The Role of Rolling Resistance in the Rheology of Wizarding Quidditch Ball Suspensions

Enzo d'Ambrosio¹, Donald L. Koch ¹ and Sarah Hormozi ¹†

¹Robert Frederick Smith School of Chemical and Biomolecular Engineering, Cornell University, NY 14853, USA

(Received xx; revised xx; accepted xx)

To elucidate the effect of particle shape on the rheology of a dense, viscous suspension of frictional, non-Brownian particles, experimental measurements are presented for suspensions of polystyrene particles with different shapes in the same solvent. The first suspension is made of spheres while the particles which compose the second suspension are globular but with flattened faces. We present results from steady shear and shear-reversal rheological experiments for the two suspensions over a wide range of stresses in the viscous regime. Notably, we show that the rheology of the two suspensions is characterized by a shear-thinning behavior, which is stronger in the case of the suspension of globular particles. Since the shear-reversal experiments indicate an absence of adhesive particle interactions, we attribute the shear thinning to a sliding friction coefficient which varies with stress as has been observed previously for systems similar to the first suspension. We observe that the viscosity of the two suspensions is similar at high shear stress where small sliding friction facilitates particle relative motion due to sliding. At lower shear stress, however, the sliding friction is expected to increase and the particle relative motion would be associated with rolling. The globular particles attain a higher viscosity at low shear stress than the spherical particles. We attribute this difference to a shape-induced resistance to particle rolling that is enhanced by the flattened faces. Image analysis is employed to identify features of the particle geometry that contribute to the resistance to rolling. It is shown that the apparent rolling friction coefficients inferred from the rheology are intermediate between the apparent dynamic and static rolling friction coefficients predicted on the basis of the image analysis. All three rolling resistance estimates are larger for the globular particles with flat faces than for the spherical particles and we argue that this difference yields the stronger shear thinning of the globular particle suspension.

Key words: Rheology, Non-Brownian frictional suspension, crushed particles, globular particle shape, irregular polygonal shape, viscosity, shear-thinning, jamming, sliding friction coefficient, rolling friction coefficient, eccentricity, shear reversal

1. Introduction

Non-Brownian suspensions made of relatively rigid particles are ubiquitous in industry (fresh concrete, civil engineering, rocket fuel, etc.) and in natural flows (mud, lava flows, submarine avalanches, etc.). This widespread occurrence has encouraged active research







FIGURE 1. Schematic of different types of 2D-projected particle shapes (from the left to the right): a simple sphere (disc), a regular polyhedron (polygon) and a globular/crushed particle which possesses flat faces and spherical arcs.

in the past years that has revealed great complexity in the behavior of these systems, which are usually composed of particles with irregular shape. Notably, it has been shown that even the simplest suspension, a non-Brownian suspension made of relatively rigid, single-sized rough spheres (of radius a) with negligible colloidal forces (no adhesion), suspended in a density-matched (no effect of gravity) Newtonian fluid (of viscosity η_0) and sheared in a viscous creeping flow (no inertial effect), can exhibit a rich variety of rheological behaviors. The best known feature is obviously the divergence of shear viscosity, η , when the solid volume fraction, ϕ , tends to a maximum value known as the jamming volume fraction, ϕ_m . But the range of complex rheological behaviors can also include the occurrence of a yield stress (Ovarlez et al. 2015; Dagois-Bohy et al. 2015), shear-thinning (Vázquez-Quesada et al. 2016; Lobry et al. 2019) or shear-thickening behaviors (Barnes 1989; Mari et al. 2014; Guy et al. 2015; Comtet et al. 2017; Madraki et al. 2017, 2018, 2020), normal stress differences, irreversibility under oscillating shear (Pine et al. 2005; Blanc et al. 2011a), shear-induced microstructure (Gadala-Maria & Acrivos 1980; Blanc et al. 2011a, 2013) and particle migration (Phillips et al. 1992; Snook et al. 2016; Sarabian et al. 2019; Rashedi et al. 2020).

Because of the complexity already present in the "simplest system", suspensions made of spheres have been extensively studied for decades. In contrast, the role played by the particle shape has only started to be investigated recently and still suffers from a dearth of experimental data. Yet, many suspensions found in industry and in nature are composed of globular particles, which have an irregular compact form with a global aspect ratio close to 1 (see Figure 1). These particles are predominantly convex due to erosion. The present paper describes an experimental work which aims at reducing this deficit, by studying the rheology of a viscous non-Brownian frictional suspension made of globular particles $(2a \sim 40\mu m)$ and comparing it with a suspension of spheres made of the same solid material and suspended in the same solvent. For this purpose, some polystyrene (PS) beads have been crushed, while others have not, in order to create two similar suspensions (described in § 2): one made of beads (see the first sketch from the left in Figure 1) and the other made of particles with irregular globular shapes (see the third sketch from the left in Figure 1). Since the recent works of Le et al. (2023) have shown that the rheology of a suspension depends strongly both on the type of particles and the solvent, it is important to note that both types of PS particles studied in the present paper are separately dispersed in the same suspending liquid (Silicone oil). Therefore, the only difference between the two types of suspension studied in the present paper is the solid particle shape and we investigate the role of shape disentangled from other factors.

In the last decade, the central role played by direct solid contact in the flow properties of non-Brownian frictional suspensions has been revealed by Boyer et al. (2011) who succeeded in applying a granular paradigm to describe the rheological behavior of non-Brownian and "non-colloidal" spheres suspended in a Newtonian fluid in the dense regime, showing the key role played by solid contact interactions between particles, existing thanks to their asperities. Later, Gallier et al. (2014) have extensively studied through a discrete element method (DEM)-like approach the influence of asperity height, h_r , and sliding friction coefficient, μ_s , between spheres on the rheology of suspensions. They have notably shown that μ_s is a key parameter that governs the flow properties of frictional suspensions of spheres in the concentrated regime ($\phi > 0.40$). Several numerical studies (Mari et al. 2014; Wyart & Cates 2014; Gallier et al. 2014; Peters et al. 2016; Singh et al. 2018) have then shown that μ_s changes the value of the jamming volume fraction, ϕ_m . For instance, Seto et al. (2013) and Mari et al. (2014) have shown that the proliferation of frictional contacts is known to be the cause of the discontinuous shear-thickening (DST) observed in highly concentrated suspensions of spheres when the shear stress is high enough to overcome repulsive interactions between particles and push them into contact. As consequences, the authors have measured, in the case of spherical particles, a decay of ϕ_m from 0.66 to 0.58 when μ_s increases from 0 (frictionless case) to 1 (frictional), in qualitative agreement with the experimental values from the literature for frictional suspensions of spheres: $\phi_m \in [0.54; 0.62]$ Zarraga et al. (2000); Ovarlez et al. (2006); Boyer et al. (2011); Blanc et al. (2011b, 2018). Later, Peters et al. (2016) numerically found that ϕ_m decreases from 0.7 to 0.56 for the same variation of μ_s (0 $\leq \mu_s \leq$ 1), in quite good agreement with these previous works. Moreover, recent experimental studies have directly measured the values of μ_s by Atomic Force Microscopic (AFM) measurements between pairs of polystyrene beads suspended in Silicone oil (Arshad et al. 2021; Le et al. 2023). They found that $0.1 \leq \mu_s \leq 4$, which confirms the considered range of the values of μ_s in the numerical studies.

Shear-thinning is common in viscous non-Brownian suspensions (Gadala-Maria & Acrivos 1980; Zarraga et al. 2000; Vázquez-Quesada et al. 2016, 2017; Dbouk et al. 2013; Blanc et al. 2018; Gilbert et al. 2022) and can have different physical origin, depending both on the physical properties of the suspension and the range of applied shear stress, Σ_{12} . By studying a non-Brownian suspension made of polyvinyl chloride (PVC) particles suspended in a 1,2-Cyclohexane dicarboxylic acid diisononyl ester (DINCH, Newtonian oil), Chatté et al. (2018) have notably put forward the possible existence of two successive regimes of shear-thinning behavior separated by a shear-thickening regime related to the frictionless-frictional transition. The first shear-thinning regime occurs at small stress, when the suspension remains frictionless since repulsion prevents direct solid particle contacts. This system can be actually seen as a suspension of "soft" particles, composed of a "hard core" (of diameter d = 2a) to which a frictionless jacket of thickness, ξ , is added. The gap 2ξ between neighboring particles is determined by balancing the normal force F_N induced by the applied stress with the colloidal repulsive force, f_N . When Σ_{12} (and therefore the normal force F_N between particles) increases, ξ decreases - and so, the apparent size of the particles decreases, $a_{app} = a + \xi(f_N)$ inducing a decay of the apparent volume fraction of the suspension and, in fine, a decay of η (Krieger 1972; Maranzano & Wagner 2001a). When the particle pressure increases more and overcomes the repulsive forces $(F_N \ge f_N^C)$, the particles enter more and more frequently into direct solid contact thanks to their asperities and the suspension passes from a frictionless state to a frictional one.

Interestingly, Mari et al. (2014) have shown that the onset of this frictionless-frictional transition ("fft") occurs for a critical shear stress (and not a shear rate, $\dot{\gamma}$):

 $\sigma_{in}^{fft} \approx 0.3 \times f_N^C/(6\pi a^2)$ for spheres, whose value is independent of ϕ as already observed in many experiments (Frith et al. 1996; Bender & Wagner 1996; Maranzano & Wagner 2001 a,b; Lootens et al. 2005; Fall et al. 2010; Larsen et al. 2010; Brown & Jaeger 2012, 2014). The authors have also shown that the stress range over which thickening occurs remains constant. This has motivated us to control the applied shear stress in the present study, instead of the shear rate. Once the load F_N is large enough $(F_N >> f_N^C)$, the direct solid contacts between particles saturate since all the particles in the suspension have contacts with their neighbors: the system is in the frictional state. Mari et al. (2014) have measured the occurrence of this second regime at Σ_{12} equal to $\sigma_{out}^{fft} \sim f_N^C/a^2$.

In the frictional state, if Σ_{12} increases further, then a potential second shear-thinning regime can be observed. We want to emphasize that it is precisely this second shearthinning regime (when the suspension is frictional) that will be explored in the present paper. The physical origin of this complex behavior remains an open question. For instance, Acrivos et al. (1994) suggest that the apparent shear-thinning behavior observed in Couette flow can be due to a difference of density, $\Delta \rho$, between the solid particles and the suspending fluid. Indeed, solid particles heavier than the suspending fluid settle because of gravity and form a more concentrated layer. Then, shear-induced viscous resuspension (Gadala-Maria 1979; Acrivos et al. 1993; Zarraga et al. 2000; Saint-Michel et al. 2019; d'Ambrosio et al. 2021) tends to homogenize the suspension when Σ_{12} increases, which induces an apparent decay of the viscosity. However, while this mechanism may arise in some experiments with Couette rheometers, it cannot explain the shear-thinning behavior observed in other types of flow. For instance, in the case of a parallel plates geometry, the shear-induced viscous resuspension would tend to increase the viscosity. In addition, we will see that Σ_{12} in the present study is large enough so that gravity would not cause significant deviation from uniform volume fraction, so the effect of any shear rate dependence related to gravity is absent.

Lastly, numerical simulations (Lobry et al. 2019) and experimental studies (Chatté et al. 2018; Arshad et al. 2021; Le et al. 2023) have shown that the shear-thinning behavior observed for concentrated viscous non-Brownian frictional suspensions (i.e. beyond the DST) could be related to a sliding friction between solid particles that varies with the normal force F_N . Following the model from Brizmer et al. (2007), Lobry et al. (2019) have considered that the contact between particles is elastic and occurs only through a few hemisphere-like asperities. In these conditions and according to the Hertz theory, the elastic contact area $A_{contact}$ is proportional to $F_N^{2/3}$ which gives:

$$\mu_s = \frac{F_T}{F_N} \propto \frac{A_{contact}}{F_N} \propto F_N^{-1/3} \tag{1.1}$$

 F_T denotes the tangential force. This model is in good agreement with experimental works (Chatté et al. 2018; Arshad et al. 2021; Le et al. 2023) which have directly determined the decay of μ_s with the normal force F_N by conducting AFM measurements between pairs of particles. Arshad et al. (2021) and Le et al. (2023) have conducted AFM measurements to measure the pairwise friction between pairs of PS beads ($d \approx 40\mu m$) immersed in an aqueous liquid and silicone oil, respectively. Note that the system of suspension studied by Le et al. (2023) is the same as the one that will be studied in the present paper. The different studies (Lobry et al. 2019; Arshad et al. 2021; Le et al. 2023) done on suspensions of spherical particles have all converged to the following equation based on

the works from Brizmer et al. (2007):

$$\mu_s = \mu_s^{\infty} \times \operatorname{coth} \left[\mu_s^{\infty} \left(\frac{F_N}{L_c} \right)^m \right]$$
(1.2)

 L_c corresponds to the critical normal force which scales the saturation of μ_s . In other words, the sliding friction coefficient becomes constant and equal to μ_s^{∞} when $F_N >> L_c$, because of an elastic to plastic transition of asperities deformation (Lobry et al. 2019). In the case of a contact between a perfectly smooth half sphere and a flat surface, Brizmer et al. (2007) determined: $\mu_s^{\infty} = 0.27$ and m = 0.35, while Lobry et al. (2019) estimated $L_c = 20 \, nN$ based on the material properties (PS particles). More recently, Arshad et al. (2021) directly measured $\mu_s^{\infty} = 0.18$ by AFM measurements and determined $L_c = 33.2 \, nN$ and m = 0.54 by fitting their experimental results obtained for PS particles in an aqueous liquid by eq.(1.2). On the other hand, Le et al. (2023) measured for PS beads in silicone oil: $\mu_s^{\infty} = 0.15$ (m = 0.4). Note that, since the particles of the suspensions studied in the present paper are of the same chemical composition found in these studies from the literature (and even the same solvent for Le et al. (2023)), we will reuse eq.1.2 coupled with the latter constants to characterize the shear-thinning behavior of the studied suspensions.

Lobry et al. (2019) have numerically determined the relationship between the normal force applied on spherical particles and the shear stress: $F_N = 6\pi a^2 \Sigma_{12}/1.69$. Equivalently, a critical shear stress, Σ_c , can be defined as: $L_c = 6\pi a^2 \Sigma_c/1.69$, which allows one to obtain the following updated equation for the variable sliding friction coefficient:

$$\mu_s = \mu_s^{\infty} \times \operatorname{coth} \left[\mu_s^{\infty} \left(\frac{\Sigma_{12}}{\Sigma_c} \right)^m \right]$$
(1.3)

It is known in granular media that the two possible motions for a particle are sliding (characterized by μ_s) and rolling. The one offering the least resistance will be favored but both can obviously occur at the same time in a sheared suspension (Estrada et al. 2008). One can easily understand that the particle shape might have a significant effect on one or even both of these motions, depending on the contact between particles. A decade ago, the numerical simulations of Estrada et al. (2011) in granular media have shown that the way a non-spherical shape provides resistance to rolling can be essentially modelled by approximating the non-spherical particle (like a globular one) by a sphere "equipped" with an apparent rolling resistance torque, Γ_{F_N} (see Figure 2). This shape-induced rolling resistance would be therefore characterized by a rolling friction coefficient, μ_r , defined from a Coulomb's type law:

$$F_N^t \leqslant \mu_r F_N$$
 (1.4)

This is the sense in which we will consider rolling friction in the present paper. It is important to note that the main assumption that we will make in the present paper will be then to approximate the 3D globular particles (irregular polyhedra) by their 2D-projected shapes (irregular polygons).

Recent numerical simulations from Singh et al. (2020) have notably predicted a decay of ϕ_m when μ_r increases, but a dearth of experimental data remains preventing verification of this important insight. Thus, in the present paper, after describing the experimental process in § 2, we will first aim (in § 3) at measuring the jamming volume fraction, ϕ_m , of the two studied suspensions, in order to characterize the rheological behavior of non-Brownian viscous suspensions made of frictional particles with irregular

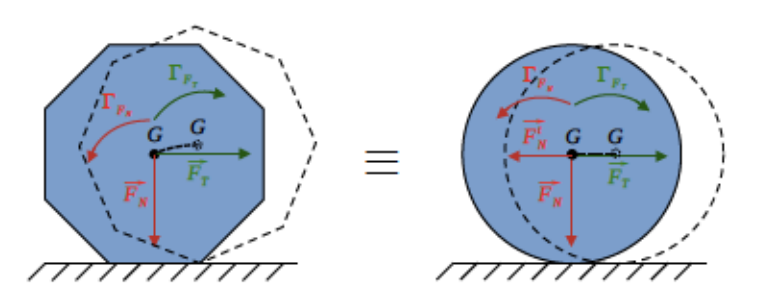


FIGURE 2. Schema of rolling on a plane from the left to the right for a regular octagon (on the left) and a disc (on the right), thanks to a tangential force, $\overrightarrow{F_T}$, applied at the center of mass G of the particles. The two particles have the same perimeter. The two systems can be considered equivalent if the disc is "equipped" with a rolling resistance torque, Γ_{FN} , directly related to a "rolling resistance force", $\overrightarrow{F_N}$ defined from the normal force, $\overrightarrow{F_N}$, applied on G as: $F_N^t \leq \mu_T F_N$. μ_T is the rolling friction coefficient (Estrada et al. 2008, 2011).

shapes and compare it with the rheology of a basic suspension made of spheres of the same material. In the second part, we will then determine by image analysis process (see § 4) the rolling friction coefficient, μ_r , of the studied globular particles in order to compare the numerical predictions of ϕ_m from the literature with our own experimental data.

2. Experimental methods

2.1. Suspensions

In this paper, the rheological behavior of two different non-Brownian viscous suspensions are investigated. The two suspensions are very similar to one another: they are both made of the same polystyrene (PS) particles (TS40, Microbeads) with a density measured as $\rho_p = 1.06 \, g/cm^3$ and sieved between 36 and $45 \, \mu m$ in order to reduce the initially large size distribution. The solid particles are then separately dispersed in the same Newtonian silicone oil (Sigma-Aldrich) of density $\rho_f = 0.97 \, g/cm^3$ and viscosity $\eta_0 = 0.98 \, Pa.s$ measured at $T = 23^{\circ}C$. The only difference between the two suspensions is in the shape of the PS particles. For the first suspension, labelled S_{PS40} , the solid particles are spheres and to make the second suspension labelled C_{PS40} , the PS particles have been crushed by a process described in appendix A. Figure 3 shows examples of these particles captured with a basic microscope: some spherical particles are presented in Fig.3(a) while a sample of crushed ones are shown in Fig.3(b). One can already note that the population of crushed particles is slightly heteroclyte, being composed of different shapes classified from simple spheres to more facetted particles and particles having both spherical and flat surfaces (see the right most schematic in Fig.1). It is this appearance, combining spherical arcs and flat surfaces similarly to a quidditch ball (the so-called quaffle), which motivated us to choose the title for the present paper. Figure 4 displays a zoomed-in image of a sample of crushed PS particles,

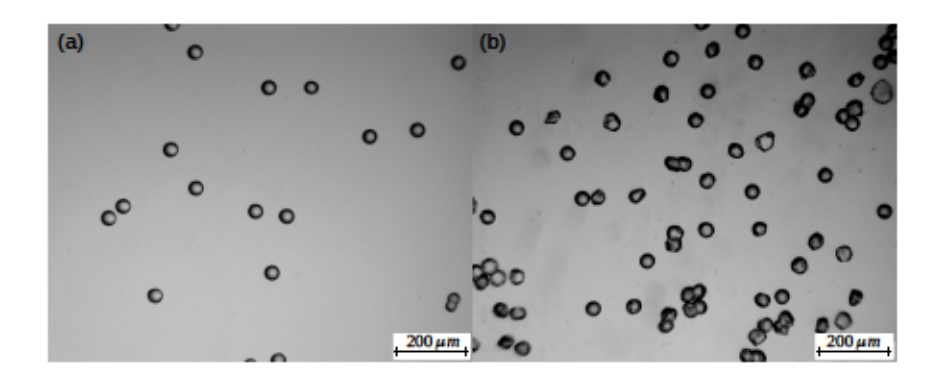


FIGURE 3. (a) Spherical PS particles. (b) Crushed PS particles. Scale $\approx 1.75\,px/\mu m$. Particle diameter : $d=2a\sim 40\mu m$.

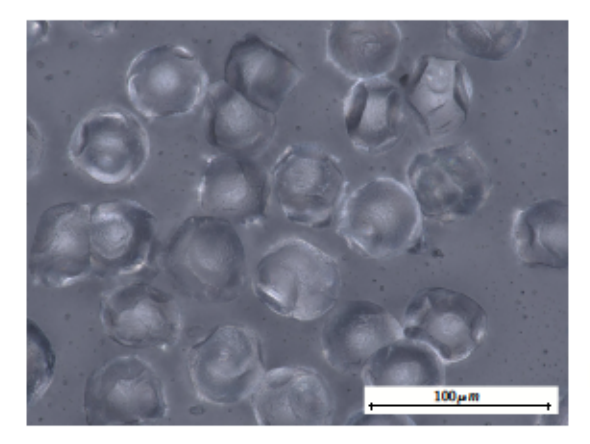


Figure 4. Globular/Crushed PS particles composing C_{PS40} .

which allows one to better appreciate this heteromorphism.

A quantitative study by image analysis has been conducted over a few hundred images captured with a microscope like the ones presented in Fig.3 in order to characterize the size distribution of the two types of particles, displayed in Figure 5. One can observe that the spherical and crushed PS particles have roughly the same size and both populations can be considered monodisperse with mean and standard deviation of the diameter of: $\langle d \rangle^{S_{PS40}} \approx (42 \pm 1) \, \mu m$ and $\langle d \rangle^{C_{PS40}} \approx (43 \pm 4) \, \mu m$.

2.2. Rheometry experiments

Rheometric experiments are carried out in a controlled-stress rheometer HR30 (TA instruments) with a smooth rotating parallel plate of radius $R=20\,mm$. The temperature is controlled by the static lower plate and is set at $T=23^{o}C$ for all the experiments. The gap is imposed at $1\,mm \lesssim h \lesssim 2\,mm$, which allows one to have enough particles (20 $\lesssim h/d \lesssim 50$) to minimize phenomena of layering and sliding. The preference of working in a parallel rotating disk is led by the near absence of shear-induced particle migration in such

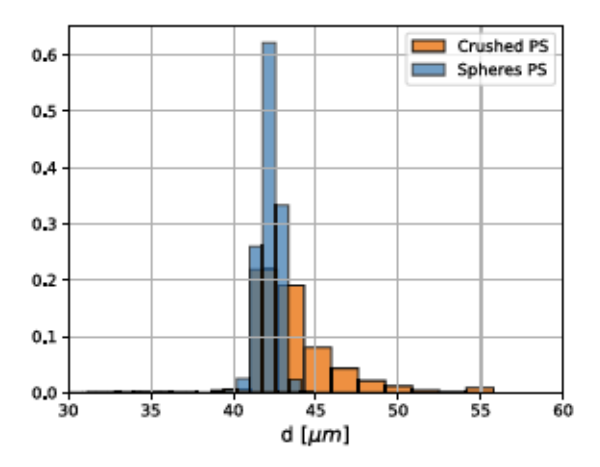


FIGURE 5. Size distribution of spheres (blue) and crushed particles (orange). For a crushed particle, the projected area, denoted A_p , is measured by microscopic image analysis. The diameter d corresponds to the diameter of a disc having the same area as the projected crushed particle: $d = 2 \times \sqrt{A_p/\pi}$.

a geometry (Chow et al. 1994; Merhi et al. 2005), which helps in keeping a homogeneous suspension across the gap. However, the drawback of this geometry is that the shear rate is not constant. Indeed, $\dot{\gamma}$ increases from 0 at the center to $\dot{\gamma}_R = \Omega R/h$ at r=R, with Ω the angular velocity of the upper rotating plate. In the case of a non-Newtonian behavior, this variation can be problematic since the viscosity of the suspension, η , depends on the shear rate, $\dot{\gamma}$. In order to take into account this experimental bias and deduce the correct values of η , we use the well-known Mooney-Rabinovitch correction:

$$\eta = \eta_{app} \left[1 + \frac{1}{4} \frac{\mathrm{d} \ln(\eta_{app})}{\mathrm{d} \ln(\dot{\gamma}_R)} \right]$$
(2.1)

 η_{app} is the apparent viscosity deduced by the rheometer from the measurements of shear rate at the rim of parallel plates, $\dot{\gamma}_R$, and applied torque, Γ :

$$\eta_{app} = \frac{2}{\pi R^3} \frac{\Gamma}{\dot{\gamma}_R}$$
(2.2)

We studied the rheological behavior of each suspension over a wide range of shear stress, $\Sigma_{12} \in [5, 100] \, Pa$, and solid volume fraction, $\phi \in [0.43, 0.51]$. For each Σ_{12} and each ϕ - in total, 50 combinations of (ϕ, Σ_{12}) -, a shear reversal experiment was performed. We encourage the readers to consult Blanc et al. (2018) for details on the protocol. Briefly, the suspension is simply sheared at a given constant Σ_{12} . Once the steady state has been reached (η is constant), the flow direction is reversed while the value of Σ_{12} is kept constant. Then, the suspension is sheared in this new direction until the steady value of η is retrieved. For each ϕ on both types of suspension, a series of shear-reversal experiments was performed on two independent samples. The results shown below correspond to the average of these two independent measurements.

Within these conditions, the values of the Péclet and Reynolds numbers characterize the suspension as non-Brownian and its flow as viscous (inertial effects are negligible), respectively:

$$Pe = \frac{6\pi \Sigma_{12}a^3}{k_BT} > 10^8$$
 and $Re = \frac{\rho_f \Sigma_{12}h^2}{\eta_0^2} < 0.1$ (2.3)

with k_B the Boltzmann constant. At the same time, note that the Stokes number is kept small throughout all the experiments: $St = \left(\frac{1}{18}\right) \frac{\rho_p d^2 \Sigma_{12}}{\eta^2} < 10^{-5}$. It is thus expected that only viscous and contact forces govern the suspension behavior.

The maximum shear stress ($\Sigma_{12} = 100\,Pa$) is set by the occurrence of edge fracture which is expected for a first normal stress of the order of the capillary pressure (Keentok & Xue 1999): $N_1 \approx 2\gamma_{\rm air-oil}/h$, with the surface tension of silicone oil, $\gamma_{\rm air-oil} \approx 30\,mN.m^{-1}$. Since the literature shows $N_1 \lesssim 0.5\Sigma_{12}$, we obtain the following criterion to avoid edge fracture: $\Sigma_{12} \lesssim 120\,Pa$, a value close to experimental observations. On the other hand, the minimum stress ($\Sigma_{12} = 5\,Pa$) is chosen in such a way that the Shield number, denoted Sh, is large enough (Sh >> 1) to ensure that the particles do not settle due to the slight difference of density, $\Delta\rho$, between the solid and liquid phases, and that a vertical homogeneous suspension is maintained throughout the entire experimental procedure:

$$Sh = \frac{\Sigma_{12}}{\Delta \rho g d} \gtrsim 10^2$$
 with $\Delta \rho = \rho_p - \rho_f = (0.09 \pm 0.02) \, g/cm^3$ (2.4)

We want to underline that AFM measurements found in the literature (Le et al. 2023) do not observe any repulsive forces before contact for PS particles (from Microbeads too) in a silicone oil (from Merck, $\rho_f = 0.95 \, g/cm^3$, $\eta_0 \approx 20 \, mPa.s^{-1}$ at $25^{o}C$), meaning that we are already in the frictional regime for the range of Σ_{12} studied in the present paper. This will be confirmed later by the measured values of ϕ_m and the comparison with the literature (Mari et al. 2014; Gallier et al. 2014; Peters et al. 2016).

To conclude this section on the rheometry, we want to emphasize that the plate surfaces are smooth and we made sure that there was no wall slip phenomenon by measuring the viscosity of the suspensions at the largest volume fraction for different gap size. A viscosity found to be independent of the height of the upper plate indicates that there is no detectable wall slip (Yoshimura & Prud'homme 1988).

3. Results and discussions on macroscopic rheological measurements

3.1. Rheological measurements

In this section, we aim to characterize the rheological behavior of the suspension made of crushed PS particles (C_{PS40}) and compare it to our measurements of the rheology of the suspension made of spherical PS particles (S_{PS40}), which is more common in the literature.

3.1.1. Steady viscosity

Figure 6 displays the variation of the measured relative steady viscosity, $\eta_r = \eta/\eta_0$, with applied shear stress, Σ_{12} , for (a) the suspension S_{PS40} made of spherical PS particles and (b) C_{PS40} made of crushed PS particles. Each colored point corresponds to an experimental measurement of η_r (relative viscosity corrected by eq.(2.1)) at a given ϕ and a given Σ_{12} . The relative uncertainty for each measurement, not represented on the graphs in Fig.6 in order to keep them clear, is always smaller than 5%.

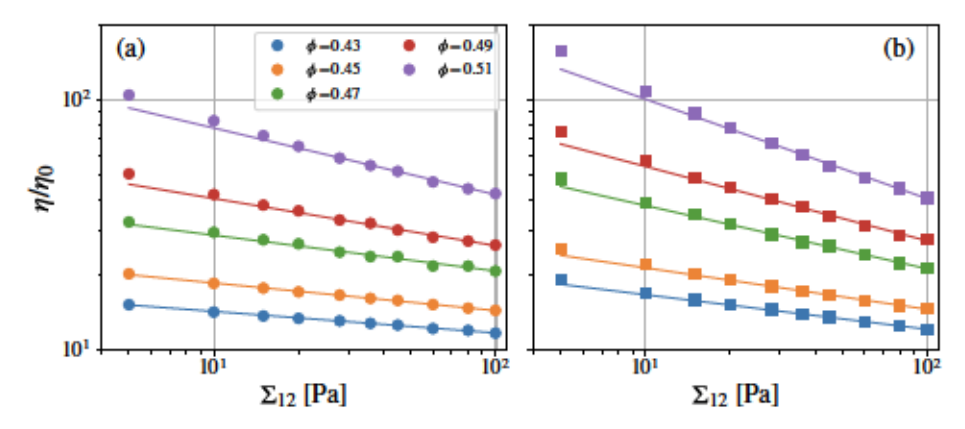


FIGURE 6. Variation of the measured relative steady viscosity, $\eta_r = \eta/\eta_0$, with applied shear stress Σ_{12} for (a) the suspension S_{PS40} made of spherical PS beads and (b) C_{PS40} made of crushed PS particles. Each color labels the solid volume fraction ϕ : 0.43 (blue), 0.45 (orange), 0.47 (green), 0.49 (red), 0.51 (purple). For each given ϕ , the experimental measurements (colored dot) are fitted by a power law (colored straight line): $\Sigma_{12} = K\dot{\gamma}^n$ with $\dot{\gamma} = \Sigma_{12}/\eta$. The resulting parameters of these fits are shown in Fig.7.

The values of viscosity measured on S_{PS40} within the explored range of Σ_{12} are in quite good agreement with other previous works present in the literature (Blanc et al. 2018; Lobry et al. 2019; Le et al. 2023) and conducted on an identical system (i.e. PS spheres of size close to $40\,\mu m$ dispersed in silicone oil). It appears in Fig.6 that C_{PS40} exhibits a rheological behavior which is broadly similar to the one which characterizes S_{PS40} . In particular, we observe for both suspensions that:

- as expected, η_r increases with φ for a given Σ₁₂.
- η_r decreases with Σ₁₂ for a given φ, qualifying the non-Newtonian behavior in the range of applied shear stress (Σ₁₂ ∈ [5 − 100] Pa) for both suspensions as shear-thinning.
- as expected, the decay of η_r with Σ₁₂ is steeper (meaning the shear-thinning behavior is more pronounced) at large φ.

On the other hand, the primary distinction between the suspensions is that the shearthinning behavior is stronger for C_{PS40} compared to S_{PS40} for a given ϕ .

According to the literature (Coussot & Piau 1994; Schatzmann et al. 2003; Sosio & Crosta 2009; Mueller et al. 2010; Vance et al. 2015), we can quantify the non-Newtonian behavior of such suspensions by fitting the experimental measurements by a power law (colored straight lines in Fig.6):

$$\Sigma_{12} = K \dot{\gamma}^n \tag{3.1}$$

K and n are the consistency factor and the shear-thinning index, respectively. Their values resulting from the fits of the experimental data in Fig.6 are displayed as functions of ϕ in Figure 7. We observe in Fig.7(a) that K increases with ϕ as expected. This reflects the increase of the viscosity with volume fraction. On the other hand, we observe in Fig.7(b) that n decreases with ϕ , which accounts for the more pronounced shear-thinning behavior at large ϕ . One can also note that n is systematically smaller in the case of C_{PS40} at a given ϕ , which reflects the more pronounced shear-thinning behavior for the suspension made of crushed particles. More precisely, we observe that the relative variation of n over the range of studied ϕ is roughly twice as large for C_{PS40} than for S_{PS40} ($\frac{\Delta n}{\langle n \rangle} \sim 0.2$ for crushed particles while $\frac{\Delta n}{\langle n \rangle} \sim 0.1$ for spheres). Regarding the

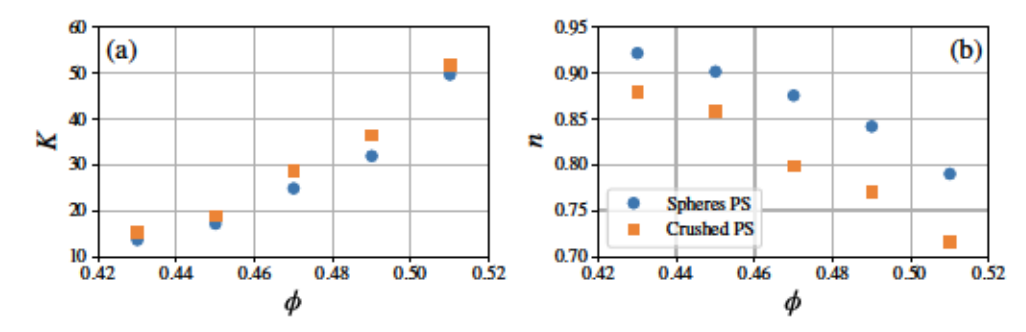


FIGURE 7. Variation of (a) the consistency factor K and (b) the shear-thinning index n with solid volume fraction ϕ for the suspensions S_{PS40} made of spherical PS particles (blue disks) and C_{PS40} made of crushed PS particles (orange squares), deduced from eq.(3.1).

consistency factor, K, it is interesting to see that apparently $K^{C_{PS40}} \approx K^{S_{PS40}}$ at a given ϕ . However, any further interpretation of this comparison in K can be difficult since its units are not exactly the same between the two suspensions because $n^{C_{PS40}} \neq n^{S_{PS40}}$ ($[K] = Pa.s^{-n}$).

From figures 6 and 7, it can be seen that the more pronounced shear-thinning behavior which characterizes the suspension C_{PS40} compared to the same suspension made of spheres (S_{PS40}) results from the observations that:

η_r^{C_{PS40}} ≈ η_r^{S_{PS40}} at large Σ₁₂ while η_r^{C_{PS40}} > η_r^{S_{PS40}} at small Σ₁₂.

To conclude this section, we would like to discuss why we have not considered the existence of a yield stress for either suspension. It is true that it is more relevant to characterize the rheological behavior for some non-Brownian suspensions by using the Herschel-Bulkley (H-B) law:

$$\Sigma_{12} = \tau_c + K \dot{\gamma}^n \qquad (3.2)$$

instead of eq.(3.1). According to the literature (Pantina & Furst 2005; Guy et al. 2018; Richards et al. 2020), it is known that the existence of a yield stress, τ_c , may be caused by the presence of weak adhesive forces between solid particles which would lead to particle aggregation. Thus, the value of τ_c may be understood as the minimum stress required to break these aggregates. Furthermore, it is expected that the crushed particles, which have some flat faces, favor Van der Waals interactions since they offer a much larger contacting surface between particles compared to spheres, leading to a higher yield stress. In view of this, we have also fitted our experimental measurements in Fig.6 by eq.(3.2). The results have shown that the impact of the third fitting parameter τ_c on K and n is negligible, since we found $\tau_c < 1 \, Pa$ for both suspensions and all explored ϕ . For S_{PS40} , one can note that this is in good agreement with the works of Le et al. (2023) who measured $\tau_c = 0.3 \, Pa$ for a very dense suspension made of PS beads having a size of $40\mu m$ and concentration $\phi = 0.55$ in a silicone oil (same system as the one studied in the present paper). The largest volume fraction studied in the present work being $\phi = 0.51$, one can expect that the values of τ_c for S_{PS40} are even smaller than this value within the range of studied ϕ . Thus, we can advance with enough confidence that the minimum applied shear stress in our study ($\Sigma_{12} = 5 Pa$) is at least 10 times larger than τ_c for S_{PS40} and C_{PS40} . We will confirm by some measurements from the shear-reversal experiments that adhesive forces do not play a significant role in the rheological behavior of the studied suspensions within the applied range of shear stress Σ_{12} .

3.1.2. A stress-dependent jamming volume fraction

We want to recall that the shear-thinning regime observed for a frictional non-Brownian suspension is common and has already been extensively observed in the literature for suspensions made of spheres (Gadala-Maria & Acrivos 1980; Zarraga et al. 2000; Dbouk et al. 2013; Vázquez-Quesada et al. 2016, 2017) or even facetted (sugar) particles (Blanc et al. 2018). As explained in the introduction of the present paper, the physical origin of this complex behavior remains an open question. Some recent works including an experimental study from Chatté et al. (2018) and numerical simulations from Lobry et al. (2019) have demonstrated that the shear-thinning behavior for frictional spheres could come from a decay of the sliding friction coefficient, μ_s , when the shear stress, Σ_{12} , increases, which induces an increase of the jamming volume fraction, ϕ_m (Wildemuth & Williams 1984; Zhou et al. 1995; Blanc et al. 2018; Lobry et al. 2019; Gilbert et al. 2022). The introduction of a stress-dependent jamming fraction $\phi_m(\Sigma_{12})$ is thus very useful to describe accurately the complex rheological behavior of a suspension. Figure 8 displays the evolution of η_s with ϕ for each applied Σ_{12} (see color code). The colored points corresponds to the experimental data and, for each applied Σ_{12} , the variation of the reduced viscosity, η_s , with the volume fraction, ϕ , is fitted by a Maron-Pierce type law:

$$\eta_s = \frac{\alpha_0}{\left(1 - \frac{\phi}{\phi_m(\Sigma_{12})}\right)^2}$$
(3.3)

Note that α_0 is used in eq.(3.3) as a second fitting parameter in order to get the most accurate fit of our experimental data. The best fit is obtained with $\alpha_0 \approx 0.85$ for both suspensions, a value close to the one used in the former Maron-Pierce equation ($\alpha_0 = 1$) and in good agreement with the numerical simulations of Lobry et al. (2019): $\alpha_0 \approx 0.8$ for $\mu_s = 0.5$ (typical value of μ_s for usual material like polystyrene). We know that the recent literature (Blanc et al. 2018; Lobry et al. 2019; Gilbert et al. 2022; Le et al. 2023) evidences a variation of α_0 with Σ_{12} (or equivalently μ_s) while we have arbitrarily chosen to impose a constant value for α_0 , independent of the considered suspension and of Σ_{12} . The main reason behind this choice is that α_0 remains a fitting parameter whose physical meaning, if any, remains an open question. Its variation with μ_s is actually only introduced to balance the variation of ϕ_m with μ_s when ϕ decreases enough and the suspension enters in the semi-dilute regime (typically $\phi \lesssim 0.3$ for a suspension of frictional spheres) (Gallier et al. 2014; Peters et al. 2016). However, when the suspension is concentrated, even though the variation of α_0 with μ_s can be large $(0.6 \lesssim \alpha_0 \lesssim 1$ for a suspension of spheres Lobry et al. 2019 or facetted particles (Blanc et al. 2018)), the values of η_s when $\phi \to \phi_m$ are controlled primarily by the value of ϕ_m . Moreover, one can note that the uncertainty in α_0 , taken into account here to fit $\eta_s(\phi)$ (see Fig.8), is kept quite large and encompasses the values from the literature: $\alpha_0 = 0.85 \pm 0.15$. Yet, it has a minimal impact on the determination of ϕ_m , as can be observed from the confidence area on the values of ϕ_m plotted for each suspension in Figure 9 (colored area).

Fig.9 displays the variation of ϕ_m with Σ_{12} for the suspensions S_{PS40} made of spheres (blue circle) and C_{PS40} made of crushed particles (orange square). As expected, we observe that ϕ_m increases with Σ_{12} for both suspensions. This increase is larger

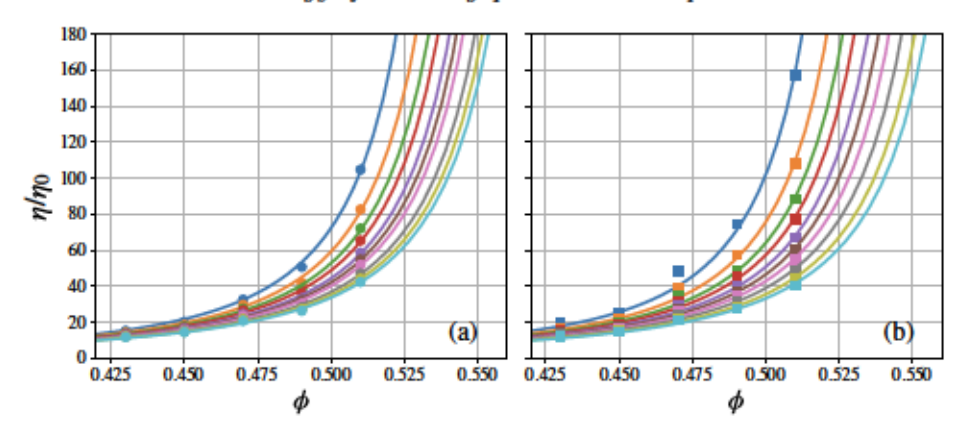


FIGURE 8. Variation of measured relative steady viscosity η_r with solid volume fraction ϕ for suspensions (a) S_{PS40} made of spherical PS and (b) C_{PS40} made of crushed PS particles. Each color labels the applied shear stress Σ_{12} : 5 (blue), 10 (orange), 15 (green), 20 (red), 28 (purple), 36 (brown), 45 (pink), 60 (grey), 80 (yellow), 100 (cyan). For each given Σ_{12} , the experimental measurements (colored dot) are fitted by a Maron-Pierce type law (see eq.(3.3)). The measurements of $\phi_m(\Sigma_{12})$ resulting from these fits are shown in Fig.9.

for C_{PS40} compared to S_{PS40} , which illustrates the more pronounced shear-thinning behavior for the suspension made of crushed particles. More precisely, we observe that:

• $\phi_m^{C_{PS40}} < \phi_m^{S_{PS40}}$ within the smaller end of the Σ_{12} range while $\phi_m^{C_{PS40}} \approx \phi_m^{S_{PS40}}$ at the largest Σ_{12} values. This mirrors the previous observation made from the viscosity comparison between the two suspensions.

For S_{PS40} , note that the values of ϕ_m range from 0.560 ± 0.005 to 0.595 ± 0.009 in very good agreement with Lobry et al. (2019), while they range from 0.550 ± 0.004 to 0.595 ± 0.009 for C_{PS40} . Globally, one can note that these values of ϕ_m for both types of suspension are in good agreement with the literature when non-Brownian frictional $(\mu_s \neq 0)$ suspensions are considered (Zarraga et al. 2000; Ovarlez et al. 2006; Boyer et al. 2011; Mari et al. 2014; Peters et al. 2016; Singh et al. 2018; Lobry et al. 2019; Singh et al. 2020). The rest of the paper will focus on finding a physical mechanism to explain the observed rheological difference between the suspension made of crushed particles and the common case of a suspension made of spheres.

3.2. Physical origin of the stronger shear-thinning regime for crushed particles

In this section, we want to understand the physical origin of the higher viscosity in the suspension of crushed particles (C_{PS40}) for small shear stress, as well as the reason that the viscosity of the two types of suspension are similar when Σ_{12} is increased. Since the only difference between the suspensions is the shape of particles present in them, it is obvious that this difference in viscosity is related to it. Two different possible physical origins will be thus investigated. Firstly, we will see in § 3.2.1 that it is unlikely that the small remaining adhesion between particles (which is expected to be stronger for the crushed particles at a given shear stress) explains this observation. Second, we will discuss in § 3.2.2 and 3.2.3 if changes in viscosity can be explained by a variable sliding friction between particles coupled with a rolling resistance of particles related to the particle shape itself. To end this section, we will study in § 3.2.4 the rheological behavior of the

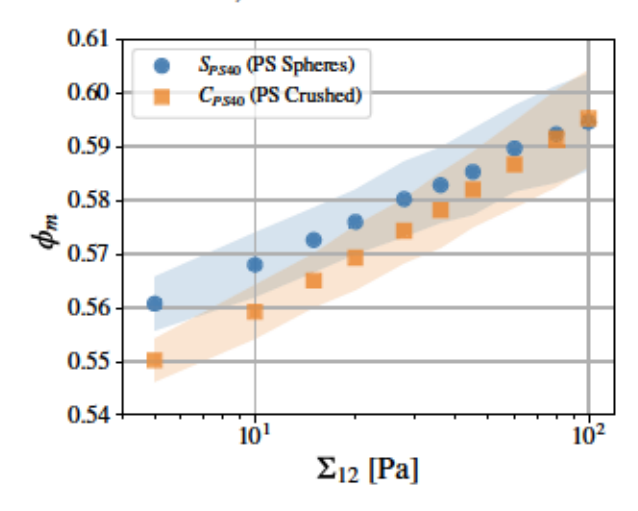


FIGURE 9. Variation of the jamming fraction ϕ_m with shear stress Σ_{12} for the suspensions S_{PS40} made of spheres PS (blue circle) and C_{PS40} made of crushed PS particles (orange square), deduced from Fig.8 and eq.(3.3) with $\alpha_0 = 0.85$. The colored area for each suspension is related to the possible range of α_0 : $0.65 \lesssim \alpha_0 \lesssim 1$.

suspensions in a frictionless case in order to confirm some assumptions of the considered model.

3.2.1. Shear reversal experiments and absence of adhesion

As mentioned previously in this paper, shear-thinning behavior of a suspension is common and can have different possible physical origins depending on the studied system (Gadala-Maria & Acrivos 1980; Zarraga et al. 2000; Vázquez-Quesada et al. 2016, 2017; Dbouk et al. 2013; Blanc et al. 2018; Chatté et al. 2018; Lobry et al. 2019; Gilbert et al. 2022). One of them is adhesion. Weak adhesive forces exist between solid particles that would lead to particle aggregation. In this scenario, two main features would appear. First, a suspension would exhibit a yield stress τ_c (Brown et al. 2010), which may be understood as the minimum stress needed to break these aggregates. Second, they would exhibit shear-thinning behavior, related to the fact that increasing Σ_{12} would break more and more aggregates, which would produce as a result a decrease in the viscosity of the suspension. Furthermore, this explanation would be suitable to explain the highest viscosity at low Σ_{12} for crushed particles while the viscosity of the two types of suspensions (S_{PS40} and C_{PS40}) would tend to be similar at large Σ_{12} . As already mentioned previously in § 3.1.1, flat surfaces of crushed particles favor particle adhesion. Potential aggregates are then less likely destroyed in C_{PS40} than in S_{PS40} when both suspensions are sheared at a given small enough Σ_{12} . This would make C_{PS40} more viscous than S_{PS40} when Σ_{12} is small. On the contrary, when $\Sigma_{12} >> \tau_c$, all the aggregates are destroyed by shear, even in the case of C_{PS40} which then flows similarly to S_{PS40} .

The first flaw in this explanation has already been presented in § 3.1.1. Indeed, we have seen that the smallest value of Σ_{12} that we apply to shear the suspension is at least 10 times larger than τ_c . At $\Sigma_{12} = 10Pa$ (second lowest value of applied shear stress), we have: $\Sigma_{12} \gtrsim 20 \times \tau_c$. Yet, a significant difference of viscosity between the two suspensions still remains at large ϕ , which raises doubt that adhesion could be the

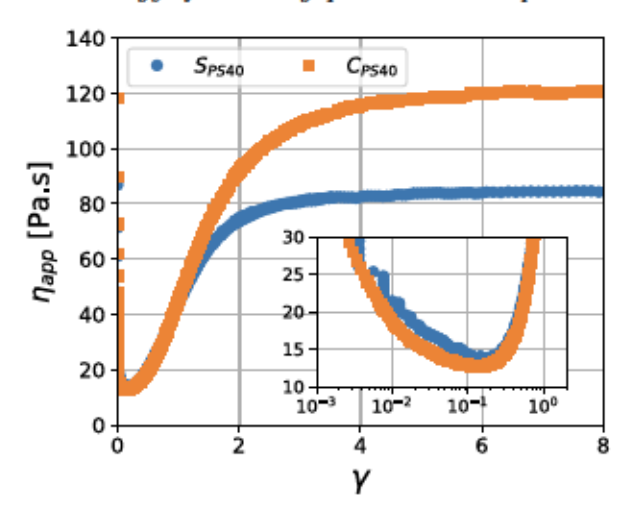


FIGURE 10. Example of transient viscosity response as a function of the accumulated strain γ during a shear reversal experiment for S_{PS40} (in blue) and C_{PS40} (in orange) with $\Sigma_{12} = 10 \, Pa$ and $\phi = 0.51$. $\gamma = 0$ corresponds to the moment when the flow is reversed. Insert: Zoom-in to better visualise the minimum value of viscosity, η_{min} reached during the transient when $\gamma = \gamma_{min}$.

main physical origin of the stronger shear-thinning for C_{PS40} . For instance, at $\phi = 0.51$ and $\Sigma_{12} = 10Pa$, $\eta_r = (110 \pm 5) Pa.s$ for C_{PS40} while $\eta_r = (80 \pm 5) Pa.s$ for S_{PS40} (See Fig.8), which gives a difference of the order of 30%. Nevertheless, we understand that this argument about Σ_{12} and τ_c alone is insufficient to support the statement that the adhesion is not mainly responsible for the more pronounced shear-thinning for C_{PS40} . It is indeed very difficult to estimate precisely when the adhesive forces can be neglect only from τ_c . To go further, we have conducted a series of shear-reversal experiments on both types of suspension by following the procedure of Blanc et al. (2018).

A shear-reversal experiment may turn out to be very interesting. It is a very basic experiment (the suspension is simply sheared at a given Σ_{12} in a given direction before the flow direction is reversed while Σ_{12} is kept constant), characterized by a very specific transient response of η which has been observed in all shear reversal experiments (Gadala-Maria & Acrivos 1980; Blanc et al. 2011a) and in simulations (Ness & Sun 2016; Peters et al. 2016). Figure 10 displays an example of the transient response of η for S_{PS40} (in blue) and C_{PS40} (in orange) at $\Sigma_{12} = 10 \, Pa$ and $\phi = 0.51$. As can be observed, a steplike drop of η occurs just after the shear reversal and the viscosity of the suspension reaches a minimum value, η_{min} , at a strain $\gamma = \gamma_{min}$ ($\gamma = 0$ corresponds to the moment of reversal). This drop is then followed by a rebound of the viscosity which reaches the steady value, $\eta_s = \eta_0 \eta_r$, it had before the shear reversal, over an accumulated strain, γ , roughly equal to $\gamma_s \sim 10$. Interestingly, the numerical simulations from Ness & Sun (2016) and Peters et al. (2016) have shown that the hydrodynamic and contact contribution to the viscosity, denoted respectively η^H and η^C , are directly connected to the values of η and η_{min} . More precisely, with $\eta_s = \eta^H + \eta^C$, Peters et al. (2016) have numerically shown in the case of a non-Brownian suspension made of (frictional or frictionless) beads the following relations:

$$\eta^C = \frac{\eta_s - \eta_{min}}{0.85/\eta_0} \qquad \& \qquad \eta^H = \frac{\eta_{min} - 0.15\eta_s}{0.85/\eta_0}$$
(3.4)

Roughly, $\eta^H \sim \eta_{min}/\eta_0$ and $\eta^C \sim (\eta_s - \eta_{min})/\eta_0$. We refer readers to the numerical work of Peters et al. (2016) to better understand the physical origin of this result. In brief, the particles in contact tend to separate when the shear is reversed. The microstructure of the suspension is thus broken, which induces the drop of the viscosity. Progressively, the microstructure of the suspension is then re-built (mirroring the microstructure before the shear reversal since the flow direction has been reversed), which induces the rebound of η to its steady value.

In the present study, the transient viscosity induced by a shear reversal can be very interesting because, if a stress-dependent particle aggregation occurs, then it should also affect the values of η_{min} and the characteristic strains, γ . Notably, Gilbert (2021) has studied the rheology of a non-Brownian frictional suspension composed of homemade soft PDMS particles (Young modulus, $E_{PDMS} = 1.8 \, MPa \, << E_{PS} \sim 3 \, GPa$) suspended in Span 80 (Newtonian liquid). By using the JKR theory (Johnson et al. 1971), the author has observed for this suspension that adhesion plays a role if $\Sigma_{12} \lesssim \tau_a \approx 10 \, Pa$. By doing shear reversal experiments, he has then shown (see Figure 86-2 of Gilbert (2021)) that $\eta_{min}^{\Sigma_{12} < \tau_a} >> \eta_{min}^{\Sigma_{12} > \tau_a}$ and, that the characteristic deformation of the transient response for a shear reversal, γ_s , was much larger than 10 ($\gamma_s \sim 50$ for $\phi = 0.4$ and $\Sigma_{12} = \tau_a$ in the case of his suspension).

Figure 11 displays the experimental measurements (colored symbols) of η_{min}/η_0 within the studied range of Σ_{12} for (a) S_{PS40} and (b) C_{PS40} , and one can see it is not similar to what has been observed by Gilbert (2021) for a non-Brownian suspension made of adhesive beads. First, $\eta_{min}^{C_{PS40}} \approx \eta_{min}^{S_{PS40}}$ at a given Σ_{12} and a given ϕ . Second, η_{min} is weakly dependent on Σ_{12} for a given ϕ in the studied range of applied shear stress. Thus, it is likely that $\Sigma_{12} >> \tau_a$ for both suspensions in the present study and that adhesion can then be neglected. We also want to underline that, based on eq.(3.4), we can determine $\eta^H \approx 5-6$ for S_{PS40} concentrated at 45% from the experimental data (roughly independent of Σ_{12}), which is in very good agreement with numerical simulations from Gallier et al. (2014) which shows $\eta^H \approx \eta_{\infty} \approx 5-6$ for a non-Brownian viscous suspensions of (frictionless or frictional) spheres at $\phi = 0.45$. η_{∞} is the high-frequency dynamic viscosity (Van der Werff & De Kruif 1989).

Note that, in Fig.11, the experimental data for η_{min} of each suspension for $\Sigma_{12} \leqslant 45 \, Pa$ have been then fitted by a power law, based on eq.(3.1) where now $K \equiv K_{min}$ and $n \equiv n_{min}$, to quantify these observations of η_{min} . The fitting parameters K_{min} and n_{min} resulting from this fit are presented in Figure 12. The upper limit for the shear stress considered here for the fit $(\Sigma_{12}^{max} = 45 \, Pa)$ is imposed due to the poor resolution of the measurement of η_{min} when $\Sigma_{12} > \Sigma_{12}^{max}$. Thus, the apparent plateau of η_{min} observed at large Σ_{12} has no physical meaning. It is an experimental artifact. Therefore, one can clearly see in Fig.12 that η_{min} for the suspensions S_{PS40} and C_{PS40} are characterized by the same rheology, as we observe that both K_{min} and n_{min} are independent of the considered suspension. Besides, S_{PS40} and C_{PS40} are both characterized by a Newtonian behavior when $\eta = \eta_{min}$: $0.94 \lesssim n_{min} \lesssim 1$ for both suspensions, when $0.43 \leqslant \phi \leqslant 0.51$ and $5 \leqslant \Sigma_{12} \leqslant 100 \, Pa$. Moreover, the η_{min} results indicate that hydrodynamic interactions are not significantly affected by particle shape.

Figure 13 displays the experimental values of characteristic strains, γ_{min} (open symbols) and $\gamma_{0.5}$ (closed symbols) for the suspension made of PS spheres (blue) and the one made of crushed particles (orange), as function of ϕ when $\Sigma_{12} = 10 \, Pa$. While

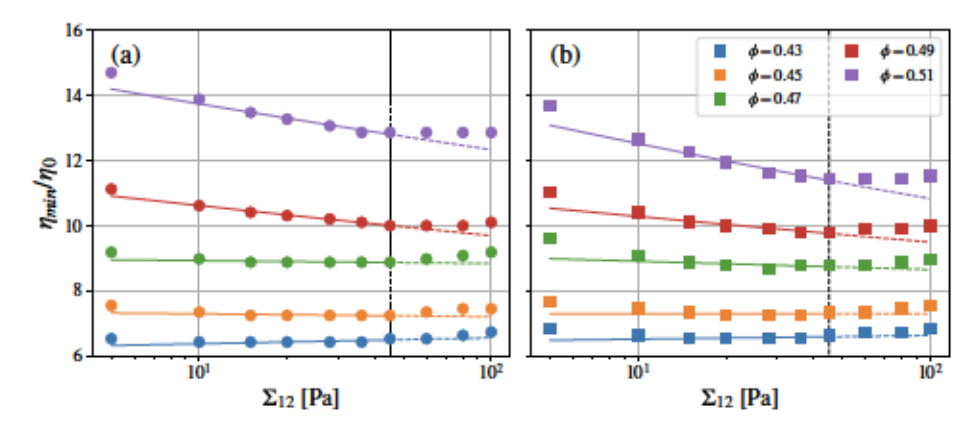


FIGURE 11. Variation of the measured relative minimum value of the viscosity, η_{min}/η_0 , with applied shear stress Σ_{12} for (a) the suspension made of spherical PS and (b) the one made of crushed PS particles. The color code labels the solid volume fraction ϕ of the suspension in the same way as in Figure 6. For each given ϕ , the experimental measurements (colored symbols) for $\Sigma_{12} \leq 45 \, Pa$ are fitted by a power law (colored straight line) : $\Sigma_{12} = K_{min} \times \dot{\gamma}^{\nu_{min}}$ with $\dot{\gamma} = \Sigma_{12}/\eta_{min}$. The parameters resulting from these fits are shown in Figure 12.

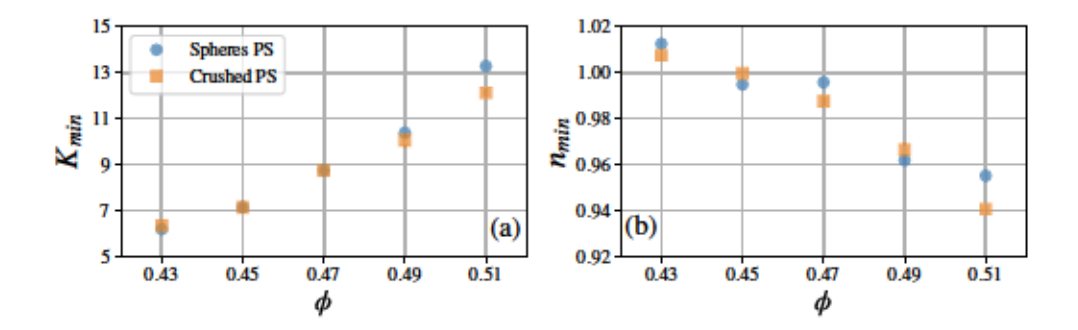


FIGURE 12. Variation of (a) the consistency factor, denoted K_{min} , and (b) the shear-thinning index, denoted n_{min} , with the solid volume fraction ϕ for the suspension made of spherical PS particles (blue disks) and the one made of crushed PS particles (orange squares), when $\eta = \eta_{min}$ and $\Sigma_{12} \leq 45Pa$.

 γ_{min} corresponds to the accumulated strain from the moment of shear reversal to when $\eta = \eta_{min}$, $\gamma_{0.5}$ is defined as the accumulated strain from the minimum state ($\eta = \eta_{min}$) to the moment when the viscosity has recovered 50% of its reversal-induced deficit:

$$\eta(\gamma_{0.5}) = \eta_{min} + 0.5 \times (\eta_s - \eta_{min})$$
(3.5)

The uncertainties of the experimental measurements for the characteristic strains are estimated at $\pm 5 \times 10^{-2}$. The experimental data are also compared with numerical (Pine et al. 2005; Peters et al. 2016) and experimental (Pine et al. 2005) results from the literature.

One can observe that γ_{min} decreases with ϕ for both suspensions and that $\gamma_{min}^{C_{PS40}} \sim \gamma_{min}^{S_{PS40}}$ for a given ϕ . A closer examination shows that $\gamma_{min}^{C_{PS40}}$ is nearly equal to $\gamma_{min}^{S_{PS40}}$ at the highest volume fraction ($\phi = 0.51$) while it is smaller than $\gamma_{min}^{S_{PS40}}$ at smaller volume fractions with the largest difference occurring $\phi = 0.43$, the lowest

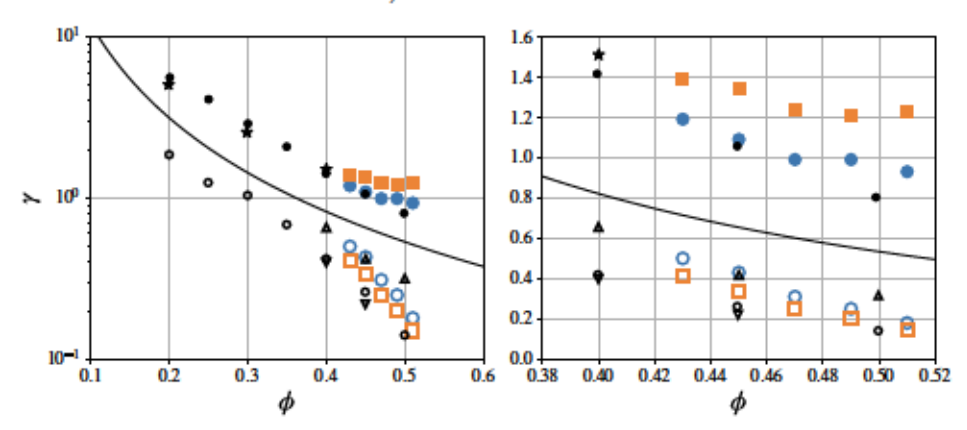


FIGURE 13. Characteristic strains γ_{min} for the minimum viscosity (open symbols) and $\gamma_{0.5}$ for the partial recovery (filled symbol) as a function of volume fraction ϕ . The graph on the right is just a zoom-in of the left one. The experimental measurements ($\Sigma_{12}=10\,Pa$) from this study are represented for the suspensions S_{PS40} (blue discs) and C_{PS40} (orange square). From the literature, Peters et al. (2016) have performed several numerical simulations to study the influence of the sliding friction coefficient μ_s and the relative roughness h_r/d on γ_{min} and $\gamma_{0.5}$. Some of their results are also plotted (black symbols) on the graph for $h_r/d = 10^{-2}$: (Δ) $\mu_s = 0$; (∇) $\mu_s = 0.5$; (∇) $\mu_s = 1$. Some experimental measurements (\star) from Pine et al. (2005) of the critical strain γ_c for which irreversibility occurs are also plotted, as well as the power law (-) resulting from their numerical simulations: $\gamma_c = 0.14\phi^{-1.93}$.

volume fraction studied. Furthermore, one can note that the experimental data are well-predicted by the simulations from Peters *et al.* (2016), conducted on a non-Brownian suspension of frictional spheres, characterized by a combination of a sliding friction coefficient, $0 \le \mu_s \le 1$, and a relative roughness height, $h_r/d = 10^{-2}$.

Analogous to γ_{min} , we observe that $\gamma_{0.5}$ decreases when ϕ increases, which is in good agreement with the literature. In addition, the experimental values for S_{PS40} at $\Sigma_{12} = 10 \, Pa$ (filled blue discs) are well-captured by the numerical simulations from Peters et al. (2016) ($\mu_s = 0.5$, $h_r/d = 10^{-2}$). One can also note that $\gamma_{0.5}^{C_{PS40}} \gtrsim \gamma_{0.5}^{S_{PS40}}$ for a given ϕ even though both are still of the same order and follow the same trend. This slight difference is interesting for two different reasons. First, as we have seen from the work of Gilbert (2021), having $\gamma_{0.5}^{C_{PS40}} \sim \gamma_{0.5}^{S_{PS40}}$ (and $\gamma_s \sim 10$ as can be observed in Fig.10) is consistent with the inference that adhesion forces do not play a predominant role in the rheology of C_{PS40} compared to S_{PS40} , within the applied range of Σ_{12} . Second, Peters et al. (2016) have explained that the force network is reestablished over a typical strain equal to $\gamma_{0.5}$ during a shear reversal experiment. According to this assertion, it would be a little harder for the particles in C_{PS40} to rearrange during the transient in order to rebuild the microstructure leading to contact forces (see the works from Peters et al. (2016) for details on the physical mechanism). We think this is related to the shape-induced rolling resistance and it could be interesting to study it by numerical simulations, since shear reversal gives access to the separate hydrodynamic and contact contributions to the stress. More generally, Peters et al. (2016) have studied the influence of μ_s and h_r/a on the values of characteristic strains and we think it could be interesting to quantify also the role played by μ_r , if any, in the transient of a shear-reversal experiment.

3.2.2. Variable sliding friction coefficient.

In the previous section, we have seen that adhesion cannot account for the shearthinning behavior of the two suspensions and that there is no evidence from shear reversal experiments of stronger adhesion in C_{PS40} than S_{PS40} . In this section, we will show that, unlike adhesion, a variable sliding friction model allows us to explain the shear-thinning behavior of the suspensions.

From the numerical works of Mari et al. (2014) and Gallier et al. (2014), it is well-known that the jamming volume fraction, ϕ_m , is strongly dependant on the sliding friction coefficient, μ_s . Besides, as presented in the introduction of the present paper, the recent literature (Chatté et al. 2018; Lobry et al. 2019; Arshad et al. 2021; Le et al. 2023) relates the shear-thinning behavior of a non-Brownian frictional suspension to a decay of μ_s when the normal force F_N between particles (directly proportional to Σ_{12}) increases:

$$\mu_s = \mu_s^{\infty} \times \coth \left[\mu_s^{\infty} \left(\frac{\Sigma_{12}}{\Sigma_c} \right)^m \right] \quad \text{with} \quad \mu_s \xrightarrow{\Sigma_{12 \to \infty}} \mu_s^{\infty}$$
 (3.6)

We recall that Σ_c is a critical value which characterizes the elasto-plastic transition of asperities deformation (Lobry et al. 2019) and μ_s^{∞} is the constant value reached by μ_s when $\Sigma_{12} >> \Sigma_c$. As for the power m, its value is directly related to the fact that the model (Lobry et al. 2019) considers that the contact between two particles occurs at only one or two asperities (mono-asperity contact) and that the particle asperities are supposed to be close to hemispheres (for which $m \sim 1/3$, Brizmer et al. 2007). Recent AFM measurements performed on PS beads ($d \approx 40\mu m$) suspended in an aqueous liquid (Arshad et al. 2021) or in silicone oil (Le et al. 2023) have given: $\mu^{\infty} \approx 0.2$, $\Sigma_c \approx 10 \ Pa$ and $m \approx 0.5$. Figure 14(a) displays the variation of μ_s with Σ_{12} based on these values (--).

Our main assumption is that eq.(3.6) can describe the variation of μ_s with Σ_{12} in both suspensions. Besides the form of the function, we assume that the values of μ_s^{∞} , Σ_c and m are also identical for both types of particles: spheres and crushed. We understand that this statement is critical but several arguments tend to support it. We recall that sliding friction should depend on the local interaction of two surfaces. In the present study, the same PS particles - in size and material - constitute the two studied suspensions and, even though the crushing process does change the radii of curvature of particles in some places, we assume that it does not significantly affect the topology of the asperities. Thus, as considered from Peters et al. (2016) for spheres, we assume that the solid contact between particles occurs through only a few asperities even to the crushed particles in C_{PS40}. In this scenario, the value of m determined by Arshad et al. (2021) and Le et al. (2023) for PS spherical particles ($m \approx 0.5$) can be applied for the crushed ones. Moreover, the values of μ_s^{∞} and Σ_c determined for PS beads ($\mu_{\infty} \approx 0.2$ and $\Sigma_c \approx 10 \, Pa$) by Arshad et al. (2021) and Le et al. (2023), depending on the properties of the solid particle material (Young's modulus E, Poisson's ratio ν , Yield strength Y_0) and asperity height h_r , can also be kept same for the crushed PS particles. We want to underline that the assumption that $\mu_s^{C_{PS40}}(\Sigma_{12}) \approx \mu_s^{S_{PS40}}(\Sigma_{12})$ is also consistent with the results displayed in Fig.13 for the characteristic strain, γ_{min} . Indeed, Peters et al. (2016) have shown the role played by μ_s on γ_{min} , and the experimental data from the present study tend to show that the values of μ_s are between 0 and 1 for the studied suspensions and are very similar between the two.

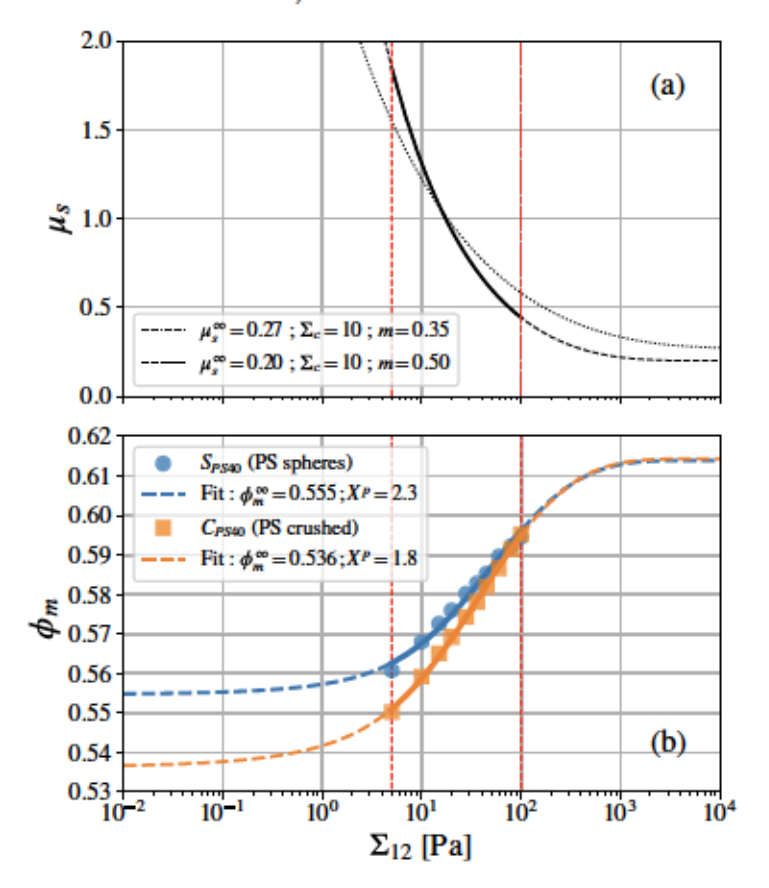


FIGURE 14. (a) Variation of the sliding friction coefficient μ_s with Σ_{12} (see eq.(3.6)) as computed by Brizmer et al. (2007) and Lobry et al. (2019) (...) and the variation used to fit the experimental data $\phi_m(\Sigma_{12})$ (--). The solid part of the curve corresponds to the experimentally studied range of Σ_{12} . (b) Jamming volume fraction ϕ_m as function of shear stress Σ_{12} . The experimental measurements for S_{PS40} (blue discs) and C_{PS40} (orange squares) are fitted by the model obtained by combining eqs.(3.6) and (3.7), where $\mu_s^{\infty} = 0.2$, $\Sigma_c = 10\,Pa$, m = 0.5 and $\phi_m^0 = 0.65$. ϕ_m^{∞} and X^p are free parameters. The best fit gives: $\phi_m = 0.555$ and $X^p = 2.3$ in the case of S_{PS40} . For C_{PS40} , we determined: $\phi_m = 0.536$ and $X^p = 1.8$. The two vertical dashed red straight lines on each graph delimit the range of Σ_{12} experimentally explored.

Lobry et al. (2019) have proposed the following phenomenological function $\phi_m(\mu_s)$ relating the jamming volume fraction to the sliding friction coefficient:

$$\phi_m = \phi_m^{\infty} + (\phi_m^0 - \phi_m^{\infty}) \left[\frac{e^{-X^p \tan(\mu_x)} - e^{-\pi X^p/2}}{1 - e^{-\pi X^p/2}} \right]$$
(3.7)

 ϕ_m^{∞} and ϕ_m^0 are specific values of ϕ_m when the particles cannot slide $(\mu_s \xrightarrow{\Sigma_{12} \to 0} \infty)$ and when the suspension is frictionless $(\mu_s \to 0)$, respectively. The expression contains a fitting parameter X^p . Fig.14(b) re-displays the variation of the jamming volume fraction, ϕ_m , with shear stress, Σ_{12} (already shown in Fig.9). In this new figure, the experimental data (represented as blue discs for S_{PS40} and orange squares for C_{PS40}) are fitted by the model described by eqs.(3.6) and (3.7). ϕ_m^{∞} and X^p are left as free parameters while ϕ_m^0 is set equal to 0.65, in good agreement with the literature when the frictionless $(\mu_s = 0)$ regime is considered (Mari et al. 2014; Gallier et al. 2014, 2018; Singh et al. 2018; Le

et al. 2023). We will see later in the present paper (in § 3.2.4) that it is also in very good agreement with the rheology of S_{PS40} and C_{PS40} sheared in the frictionless regime.

We observe that the experimental data are well-predicted by the model within the experimentally explored range of shear stress ($\Sigma_{12} \in [5-100]\,Pa$, colored solid lines in Fig.14b). By coupling Figs.14(a) and (b), one can note that $\phi_m^{PS40} \approx (0.593 \pm 0.009)$ when $\mu_s \approx 0.5$ ($\Sigma_{12} \sim 80\,Pa$) and $\phi_m^{PS40} = (0.573 \pm 0.006)$ when $\mu_s = 1$ ($\Sigma_{12} \sim 20\,Pa$) for the suspension made of spheres, which is in quite good agreement with numerical simulations from the literature. For instance, Peters *et al.* (2016) and Gallier *et al.* (2018) found $\phi_m \approx 0.59$ and $\phi_m \approx 0.58$, respectively, when $\mu_s = 0.5$. The numerical simulations of Mari *et al.* (2014) and the ones from Peters *et al.* (2016) predict $\phi_m \approx 0.58$ and $\phi_m \approx 0.56$ for $\mu_s = 1$, respectively.

Then, one can observe in Fig.14(b) that the variation of ϕ_m with Σ_{12} deduced from the fit exhibits two plateaus (--), each located at extreme values of shear stress: the first one when $\Sigma_{12} \lesssim 10^{-1} \, Pa$ and the second one when $\Sigma_{12} \gtrsim 10^3 \, Pa$. According to eq.(3.6) (Lobry et al. 2019), the plateau when $\Sigma_{12} \to +\infty$ is due to the saturation of μ_s (plastic regime) when $\Sigma_{12}/\Sigma_c >> 1$ (see Fig.14a). The other plateau predicted by the fit when $\Sigma_{12} \to 0$ is explained by the weak influence of μ_s on the values of ϕ_m when μ_s is larger than 1 or 2, as demonstrated by the numerical works of Mari et al. (2014), Peters et al. (2016) and Lobry et al. (2019).

In Fig.14(b), the function $\phi_m(\Sigma_{12})$ deduced from the fit is then characterized by:

- $\phi_m \xrightarrow{\Sigma_{12} \to 0} \phi_m^{\infty} = (0.555 \pm 0.005)$ for S_{PS40} and $\phi_m^{\infty} = (0.536 \pm 0.004)$ for C_{PS40} .
- $\phi_m \xrightarrow{\Sigma_{12} \to \infty} \phi_m^{0.2} = (0.61 \pm 0.01)$ for S_{PS40} and C_{PS40} .

Note that the estimated values of ϕ_m^{∞} and $\phi_m^{0.2}$ for S_{PS40} are in very good agreement with the literature (Fernandez et al. 2013; Mari et al. 2014; Gallier et al. 2014; Peters et al. 2016; Lobry et al. 2019; Le et al. 2023). Mari et al. (2014) and Lobry et al. (2019) determined $\phi_m \approx 0.56$ and $\phi_m \approx 0.546$ when $\mu_s \to +\infty$, respectively, while Le et al. (2023) obtained $\phi_m^{\infty} \approx 0.55$ by studying experimentally the same suspension as S_{PS40} . Peters et al. (2016) found $\phi_m \approx 0.61$ when $\mu_s = 0.3$ and Lobry et al. (2019) determined $\phi_m \xrightarrow{\Sigma_{12} \to \infty} \phi_m^{0.27} = 0.625$. Regarding C_{PS40} , one can observe that:

• $\phi_m^{\infty}|_{C_{PS40}} < \phi_m^{\infty}|_{S_{PS40}}$ and $\phi_m^{0.2}|_{C_{PS40}} \approx \phi_m^{0.2}|_{S_{PS40}}$, as expected.

To sum up, we have observed by fitting the experimental data $\phi_m(\Sigma_{12})$ by eqs.(3.6) and (3.7) that the shear thinning behavior of the two studied suspensions (S_{PS40} and C_{PS40}) is induced by the same variable friction law, $\mu_s(\Sigma_{12})$. The main difference between the two is in ϕ_m^{∞} , whose value is smaller in the case of globular/crushed PS particles compared to the PS spheres. One can note that $X^p|_{C_{PS40}} \sim X^p|_{S_{PS40}} \sim 2$, which supports the statement about the sliding friction being the same for the two types of particles. Moreover, $X^p|_{S_{PS40}} \approx 2.3$ is a value which is in good agreement with the literature (Lobry et al. 2019; Arshad et al. 2021; Le et al. 2023).

3.2.3. Geometry-related rolling resistance.

A decade ago, Estrada et al. (2008) and Estrada et al. (2011) have simulated rolling regular polygons and shown that the stress was the same as disks (with the same ϕ) equipped with a rolling friction coefficient, μ_r (see schema in Fig.2). This would then mean that the geometric effect is a rolling resistance which, in the case of equivalent disks, can be obtained with a μ_r .

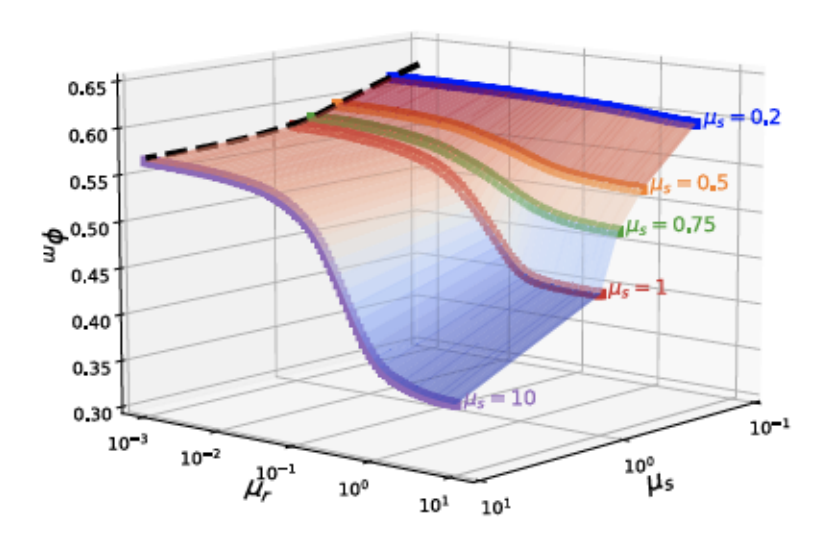
More recently, in the frame of a study characterizing the shear-thickening behavior of suspensions made of hard spheres (for which μ_s is kept constant), Singh et al. (2020) have numerically studied the role of torque-activated (or stress-activated) rolling resistance, which can be simply induced by the "rough" particle shape of particles in real-life suspensions. Note that adhesive surfaces can also induce a resistance to rolling motion but we eliminated this physical origin in § 3.2.1. To this aim, the authors have simulated spherical particles with a rolling resistance characterized by a rolling friction coefficient, μ_r . Singh et al. (2020) have then studied the role played by different combinations of μ_r and μ_s in determining the value of the jamming volume fraction, ϕ_m . As shown in Figure 15 which displays their result, Singh et al. (2020) demonstrated interestingly on the one hand that ϕ_m depends weakly on μ_r when μ_s is small enough (typically, $\mu_s \lesssim 0.35$). For instance, their results show that ϕ_m decreases from 0.62 to 0.60 when μ_r increases from 10^{-3} (vanishing rolling resistance) to 10 (extremely strong rolling resistance), and $\mu_s = 0.2$ (see blue curve in Fig.15). Note that we determined in the present work: $\phi_m = 0.61 \pm 0.01$ when $\mu_s = 0.2$ (see Fig.14), which is in very good agreement with this observation. On the other hand, Singh et al. (2020) have predicted that ϕ_m is strongly dependent of μ_r when $\mu_s \gtrsim 0.5$. For instance, within the same range of rolling friction coefficient ($\mu_r \in [10^{-3} - 10]$), the authors showed that ϕ_m decreases from 0.57 to 0.36 when $\mu_s = 10$ (see purple curve in Fig.15). Typically, this corresponds to the case where sliding is prevented and only rotation can occur $(\mu_r \ll \mu_s \to \infty)$. In the frame of the present study, this latter result from the literature (Singh et al. 2020) is very interesting since, based on the assumption that $\mu_r|_{C_{PS40}} > \mu_r|_{S_{PS40}}$, it can explain the main observation obtained in the previous section:

• $\phi_m^{\infty}|_{C_{PS40}} < \phi_m^{\infty}|_{S_{PS40}}$ and $\phi_m^{0.2}|_{C_{PS40}} \approx \phi_m^{0.2}|_{S_{PS40}}$.

To sum up, the rheology of the suspensions $(S_{PS40} \text{ and/or } C_{PS40})$ is solely determined by μ_r (induced by the non-spherical particle shape) when $\phi_m \to \phi_m^{\infty}$ ($\mu_s \xrightarrow{\Sigma_{12} \to 0} \infty$), while it is nearly independent of shape when $\phi_m \to \phi_m^{0.2}$ ($\mu_s \xrightarrow{\Sigma_{12} \to \infty} \mu_s^{\infty} = 0.2$) or $\phi_m \to \phi_m^0$ ($\mu_s \to 0$). Estrada et al. (2008) have indeed demonstrated in the frame of a numerical study on granular material that the dominant mode of relative motion at the contacts (sliding or rolling) is the one which minimizes the coefficient of internal friction. This simply means that the particles prefer rolling if $\mu_r << \mu_s$ or sliding if $\mu_r >> \mu_s$. The case where $\mu_r \sim \mu_s$ is obviously more complex since it involves rolling and sliding motion at the same time. Thus, by considering the most extreme case where $\mu_s = 10$ in Fig.15 (rolling mode) and having deduced the values of ϕ_m^{∞} for each type of suspension (see § 3.2.2), a value of the rolling friction coefficient $\mu_r^{\phi_m^{\infty}}$ for each suspension can be predicted from the rheological measurements: $\mu_r^{\phi_m^{\infty}}|_{S_{PS40}} = 0.03 \pm 0.02$ and $\mu_r^{\phi_m^{\infty}}|_{C_{PS40}} = 0.10 \pm 0.01$. Note that the uncertainty in $\mu_r^{\phi_m^{\infty}}$ for each suspension is due to the uncertainty in the value of ϕ_m^{∞} related to the possible range of α_0 (see eq.(3.3)).

3.2.4. Frictionless suspensions made with the same particles

We have briefly studied the rheology of the frictionless case ($\mu_s = 0$) of the two suspensions studied in the present paper, by dispersing the same PS particles present in S_{PS40} and C_{PS40} in an aqueous solution, labelled AQ0, and shearing the suspensions



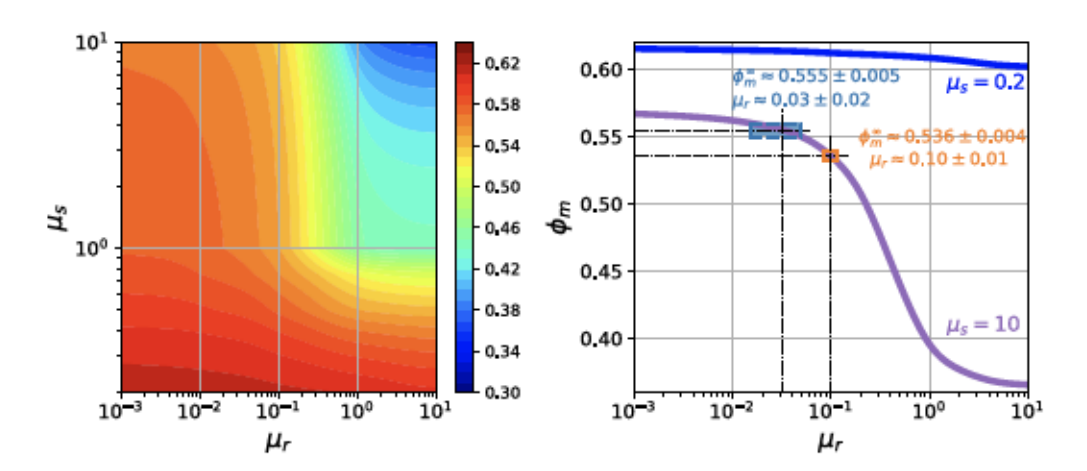


FIGURE 15. The jamming volume fraction ϕ_m as function of sliding friction coefficient, μ_s , and rolling friction coefficient, μ_r , as computed by Singh et~al.~(2020). Their data can be obtained at: https://acdc.alcf.anl.gov/mdf/detail/singh_rolling_friction_prl_2020_v1.4/. Bottom right: Variation of ϕ_m with μ_τ for $\mu_s = 0.2$ (blue) and $\mu_s = 10$ (purple). The latter allows one to predict the values of μ_τ for S_{PS40} and C_{PS40} from the experimental values of $\phi_m^{\infty}|_{S_{PS40}}$ (light blue) and $\phi_m^{\infty}|_{C_{PS40}}$ (orange), respectively: $\mu_\tau^{\phi_m^{\infty}}|_{S_{PS40}} = 0.03 \pm 0.02$ and $\mu_\tau^{\phi_m^{\infty}}|_{C_{PS40}} = 0.10 \pm 0.01$.

in a vane tool geometry. The aqueous solution is a mixture of deionized water with a small amount (less than 3 wt%) of Triton-X-100 (surfactant, Sigma Aldrich) and Sodium Iodide. We encourage the experimental reader to see the Supplementary material of Madraki et al. (2020) for more details about this experimental procedure. Furthermore,

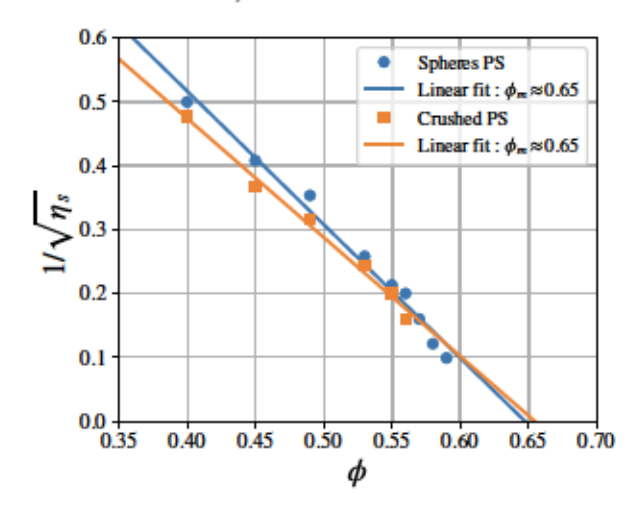


FIGURE 16. Inverse of the square root of the shear viscosity, $1/\sqrt{\eta_s}$, against volume fraction, ϕ , for two different suspensions: the first made of the same spheres as in S_{PS40} and the second made of the same crushed particles as in C_{PS40} . Here, the PS particles are dispersed in an aqueous solution ($\eta_0 = 10^{-3} Pa.s$). The two suspensions sheared at $\Sigma_{12} = 10^{-2} Pa$ in a vane tool geometry are frictionless ($\mu_s = 0$). A linear fit gives: $\phi_m \approx 0.65$ for both types of suspension.

the critical normal load f_N^C (occurrence of the frictionless-frictional transition) has been measured by AFM measurements by Madraki et al. (2020) for PS beads ($d \approx 140 \,\mu m$) in this aqueous solution AQ0. The authors found: $f_N^C = (12 \pm 4) \,\mu N$, which gives: $\sigma_{in}^{fft} \approx 0.3 \times f_N^C/(6\pi a^2) \sim 40 \,Pa$ (Mari et al. 2014) for this type of suspension (PS beads in AQ0).

Figure 16 displays the experimental measurements of η_s (colored symbol) for spherical PS particles (blue discs) and crushed PS particles (orange squares) in aqueous solution AQ0, when $\Sigma_{12} \approx 10^{-2} \, Pa$ (frictionless case: $\Sigma_{12} << \sigma_{in}^{fft} \leftrightarrow \mu_s = 0$). As expected, the variation of the reduced viscosity η_s with the volume fraction ϕ follows a Maron-Pierce law (colored solid straight lines in Fig.16, see eq.(3.3)) with $\alpha_0 = 1$ (Peters et al. 2016; Lobry et al. 2019). The result of the linear fit of $1/\sqrt{\eta_s}$ as function of ϕ gives $\phi_m \approx 0.65$ for both suspensions. Several observations can be underlined from this result:

- In the case of frictionless spherical particles, the value of 0.65 for the jamming fraction is in very good agreement with the literature (Mari et al. 2014; Gallier et al. 2018; Singh et al. 2018) and this confirms that the suspension is frictionless.
- It confirms our previous choice to have assumed $\phi_m^0 = 0.65$ in order to fit the experimental data for $\phi_m(\Sigma_{12})$ of the suspensions C_{PS40} and S_{PS40} by eqs. (3.6) and (3.7).
- Finally, φ⁰_m = φ_m|_{crushed PS in AQ0} = φ_m|_{spheres PS in AQ0} = 0.65 is consistent with the numerical results of Singh et al. (2020) who found that φ_m is independent of μ_r when μ_s → 0.

In the second part of the present paper, we will describe how we can determine a value of μ_r for each type of particles (spheres and crushed), based on image analysis. The goal is to compare these new values with the ones predicted by the combination of the numerical works of Singh *et al.* (2020) based on shear rheology measurements coupled with the experimental data $\phi_m(\Sigma_{12})$ (see in § 3.2.2 and § 3.2.3) that we recall here: $\mu_r^{\phi_m^{\infty}}|_{S_{PS40}} = 0.03 \pm 0.02$ and $\mu_r^{\phi_m^{\infty}}|_{C_{PS40}} = 0.10 \pm 0.01$.

4. Image analysis study

In this section, we will focus on the direct determination of the value of the rolling friction coefficient, μ_r , to be compared with the value, $\mu_r^{\phi_m}$, inferred from our rheological measurements and the simulations of Singh *et al.* (2020) (see Fig.15), $\mu_r^{\phi_m}$. Nevertheless, we note that the treatment of a non-spherical particle by a single rolling friction coefficient on a sphere is an approximation. It would not be exact for two reasons. One is that the resistance to rolling of the non-spherical particle would be different at different parts of the surface. The other is that the static rolling resistance one needs to overcome to initiate rolling could be larger than the time averaged dynamic rolling resistance one needs to balance to maintain rolling. This difference was minimized by Estrada *et al.* (2011) by considering a uniform polygon. We will want to determine how well either of these rolling friction coefficients helps to describe a more irregular but still compact particle rolling resistance.

4.1. Characterizing quantities of particle shape

To our knowledge, a precise measurement of μ_r between a pair of particles is much more difficult than the measurement of μ_s , which can be done by AFM measurements (Chatté et al. 2018; Arshad et al. 2021; Le et al. 2023). It is even more difficult for crushed particles with irregular shapes which require even more statistics. It is common in granular media to determine μ_r by letting a particle roll over a slope (Agarwal et al. 2021). But the determination of μ_r by this method can be very complicated or nearly impossible for small particles or particles with a large deviation from spherical shape. Because of these experimental limits, we have chosen here to use a novel method introduced by Agarwal et al. (2021) and Tripathi et al. (2021), based on image analysis of static grains to calculate the rolling friction coefficient without considering any material properties of the particle. The basic principle of this novel method is to approximate the projected image of a given particle as a polygon that we can characterize by measuring:

- the aspect ratio, a_{ratio} , defined as the ratio of the longest "height" (ie. the length between the center of mass, G, and a side V_iV_j) of the polygon over the smallest one: $a_{ratio} = h_{ij}^{max}/h_{ij}^{min}$,
 - the number of sides, n_s,
 - the internal angle of each vertex, α₁,
 - the length of each side, L_{ij}
 - the eccentricity associated with each side, |e

 if | d.

A qualitative schema of an irregular polygon is displayed in Figure 17 to help visualise the different characterizing quantities that we aim to measure. Regarding the vector $\overrightarrow{e_{ij}}$, we want to underline that: $\overrightarrow{e_{ij}} = \overrightarrow{GE_{ij}}$. As we will see later, the parameter e_{ij} , the horizontal component of $\overrightarrow{e_{ij}}$ can be negative or positive depending on the relative position of E_{ij} , G and V_j . The eccentricity is then defined as the magnitude of $\overrightarrow{e_{ij}}$.

4.1.1. Approximation of particles projected area as an irregular convex polygon

Figure 18 shows 4 examples of 2D-approximations as irregular convex polygons for the images of particles composing the suspensions S_{PS40} (a, c) and C_{PS40} (b, d). The basic images are taken with a microscope (examples of basic photos shown in Figure 3) with

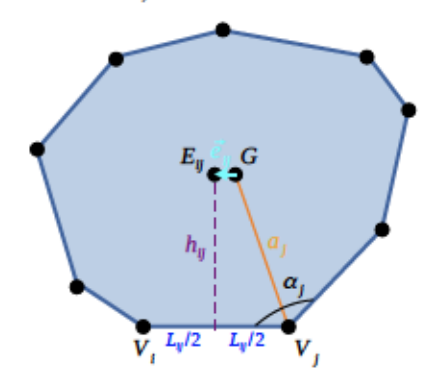


FIGURE 17. Sketch of a crushed particle (blue area), considered as an irregular convex polygon with a center of mass G. The sides of the polygon/crushed particle are outlined in a darker blue. The vertices connecting each side are displayed as dark points. L_{ij} is the length of a side connecting two successive vertices, V_i and V_j . The radius a_j is the length of the segment connecting G to the vertex V_j . h_{ij} is the height of the centroid G above the segment V_iV_j . The black point E_{ij} is on the bisector of the segment V_iV_j and at the same height h_{ij} from the segment V_iV_j as G. The eccentricity of the particle/polygon related to its side V_iV_j is defined as the ratio of the length of the vector $\overrightarrow{e_{ij}}$, denoted $|\overrightarrow{e_{ij}}|$, to the projected diameter, d.

an approximate scale of 80 pixels per particle (projected) diameter. We recall that the projected diameter, d (see Fig.5), for a crushed particle corresponds to the diameter of a sphere having the same projected area as the non-spherical particle. Note that, from the start, images with well-separated particles are captured, but if two or more particles are not distinct enough (see Fig.3), they are simply not taken into account to compute μ_r . Moreover, we want to emphasize that spherical particles, like the ones in Fig.18(a, c), are also present in C_{PS40} . In the end, the resulting characterising quantities of particles presented above are determined for approximately 600 particles for each type of particle.

The image analysis process is described in appendix B. The data for the physical particles are compared with results for 10000 "reference" numerical spheres with similar diameters as the real particles, i.e., in the range $70 \le 2a \le 90 \, px$. This comparison allows us to examine the effect of the image resolution on the properties of the particles, which in all cases are approximated as polygons.

4.1.2. Image analysis results on characteristic quantities of particles shape

Once the coordinates $(V_{i,x}, V_{i,y})$ of each vertex V_i for a given polygon/particle are known, all the characteristic physical quantities for a captured polygon/particle (see schema in Fig.17) can be determined. Particularly, the area A_p and the location (x_G, y_G) of the center of mass G of each particle/polygon are determined as follows:

$$A_p = \frac{1}{2} \sum_{i=0}^{n_s - 1} det(V_i, V_j) = \frac{1}{2} \sum_{i=0}^{n_s - 1} \left[V_{i,x} V_{j,y} - V_{j,x} V_{i,y} \right]$$
(4.1)

$$x_G = \frac{1}{6A_p} \sum_{i=0}^{n_x - 1} \left[(V_{x,i} + V_{x,j}) \det(V_i, V_j) \right]$$
(4.2)

$$y_G = \frac{1}{6A_p} \sum_{i=0}^{n_s - 1} \left[(V_{y,i} + V_{y,j}) \det(V_i, V_j) \right]$$
(4.3)

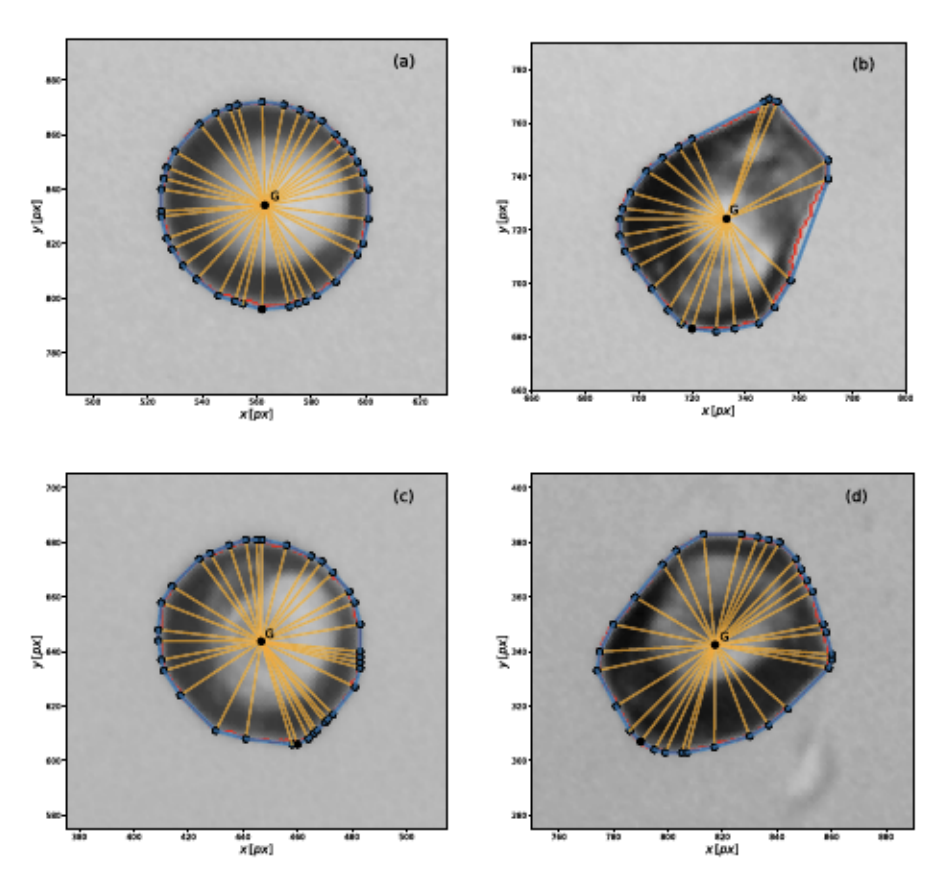


FIGURE 18. Examples of 2D-approximation by an irregular convex polygon for particles composing the suspensions S_{PS40} (a,c) and C_{PS40} (b,d). The sides of a polygon are colored in blue while the vertices are marked as black dots. The center of mass G of the polygon/particle is also located and orange straight lines connecting the centroid G to each vertex are displayed. The red pixels delimit the contour detected by the segmentation process. Scale: "diameter" of particle $\sim 80 \, px$.

with j = i + 1, except if $i = n_s - 1$ then j = 0.

In addition to the size distribution already shown in Fig.5 where we observed that crushed and spherical particles have roughly the same size ($d \sim 40 \,\mu_m$, with a slight larger degree of polydispersity for the crushed ones), Figure 19 displays the distribution of the values of characteristic physical quantities determined for the "reference" perfectly smooth spheres (in green), the real spherical particles in S_{PS40} (in blue) and the real crushed ones in C_{PS40} (in orange). One can observe that the particles from S_{PS40} (in blue) are mainly spheres since the differences from the reference data (in green) are small:

- the aspect ratio of particles in S_{PS40} is close to 1 ($a_{ratio}^{S_{PS40}} \lesssim 1.2$ with 90% of $a_{ratio}^{S_{PS40}} \lesssim 1.1$)
- the number of segments per polygon and the length of sides are comparable between the spheres from S_{PS40} and the "reference" perfectly smooth spheres $(\langle n_s^{S_{PS40}} \rangle \sim \langle n_s^{ref} \rangle \approx 35$ and $\langle L_{ij}/d \rangle^{S_{PS40}} \sim \langle L_{ij}/d \rangle^{ref} \sim 10^{-1})$
 - the angles are nearly the same $(\langle \alpha_j \rangle^{S_{PS40}} \sim \langle \alpha_j \rangle^{ref} \approx 170^o)$

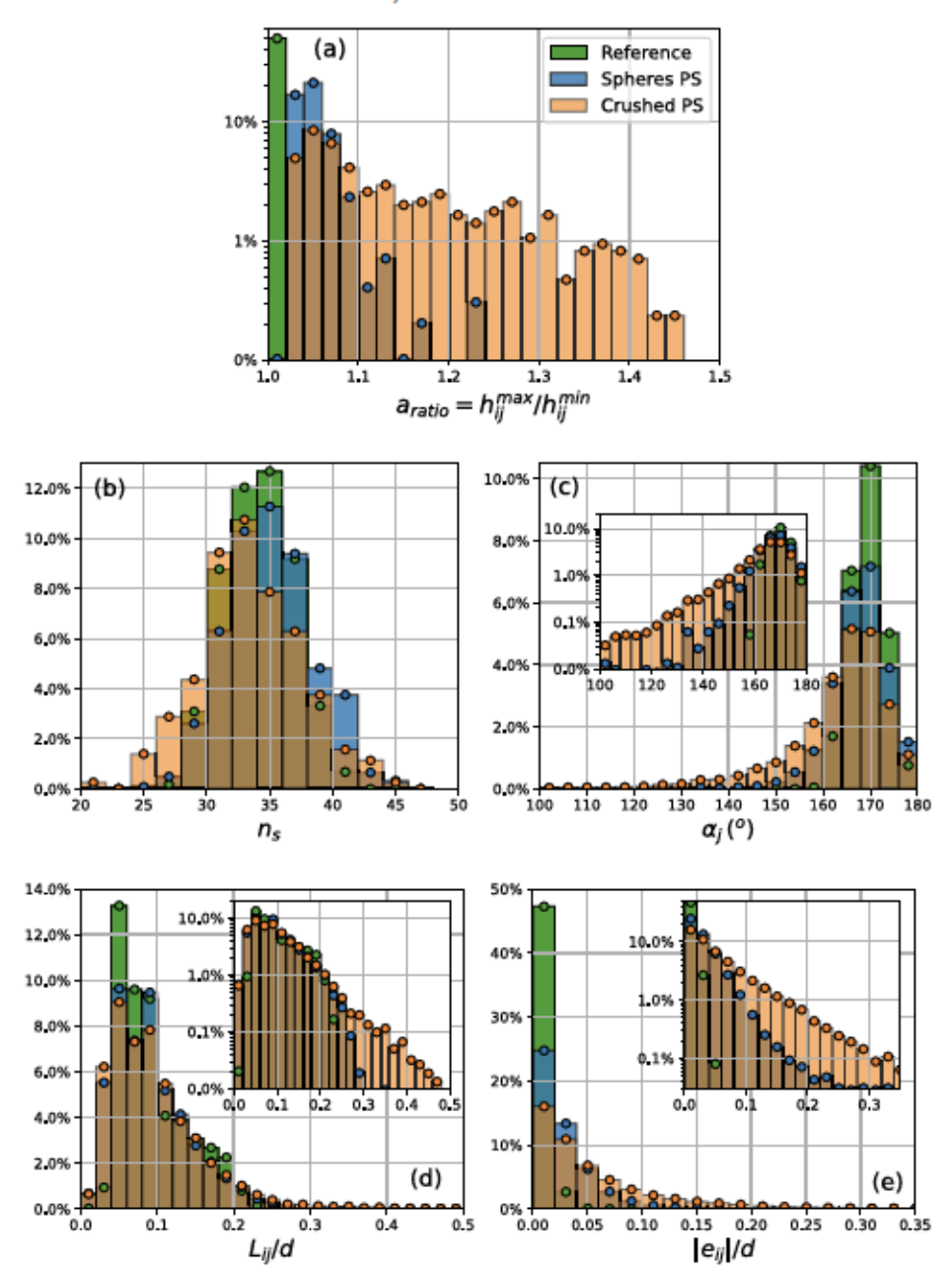


FIGURE 19. Distribution of the values of (a) polygonal aspect ratio $a_{ratio} = h_{ij}^{max}/h_{ij}^{min}$, (b) number of segment per particle n_s , (c) internal angle α_i at each vertex V_i , (d) relative length L_{ij}/d and (e) eccentricity $|\overrightarrow{e_{ij}}|/d$ measured across all the particles for the suspensions S_{PS40} (blue) ad C_{PS40} (orange). For a_{ratio} and n_s , the statistics include roughly $N \sim 600$ particles for each type of suspension while, for α_j , L_{ij}/d and $|\overrightarrow{e_{ij}}|/d$, the computation is done for all the vertices V_i of all the polygons: $\langle n_s \rangle \times N \sim 2 \times 10^4$ data for each suspension. Insert in (c) and (d): logarithmic y-scale is used to highlight the largest values of L_{ij}/d and $|\overrightarrow{e_{ij}}|/d$, respectively. The data from real suspensions are compared with the results (in green) obtained by doing the same image analysis process on a numerical image of perfectly smooth spheres that we use as reference.

- the eccentricity for the beads of S_{PS40} is very small $((|\overrightarrow{e_{ij}}|/d)^{S_{PS40}} \lesssim 10^{-1} \text{ including } 90\% \text{ of } (|\overrightarrow{e_{ij}}|/d)^{S_{PS40}} \lesssim 5.10^{-2}).$

The comparison of the "reference" spheres and the spherical particles of the suspension S_{PS40} on α_j , L_{ij} and $|\overrightarrow{e_{ij}}|/d$ allows us to characterize the slight deviation from perfect spheres, which is much less than the deviation of crushed particles from spherical shapes.

At first glance, one can observe that the global shape of crushed particles does not deviate much from a sphere. Especially, Fig.19(a) shows that $a_{ratio} < 1.5$ for crushed particles, with two-thirds of $a_{ratio}^{C_{PS40}} \lesssim 1.2$. Besides, the crushed particles from C_{PS40} and the spheres from S_{PS40} are both globally approximated as polygons notably having:

- the same number of sides since $\langle n_s^{C_{PS40}} \rangle \sim \langle n_s^{S_{PS40}} \rangle \approx 35$,
- the same global angle since $150^{\circ} \leqslant \alpha_{j} \leqslant 180^{\circ}$ for $\sim 88\%$ of $\alpha_{j}^{C_{PS40}}$ and $\sim 96\%$ of $\alpha_{j}^{S_{PS40}}$,
- the same average length of polygon sides $(\langle (L_{ij}/d)^{C_{PS40}} \rangle \sim \langle (L_{ij}/d)^{S_{PS40}} \rangle \sim 0.1)$. Moreover, the mean normalized eccentricity $\langle (|\overrightarrow{e_{ij}}|/d)^{C_{PS40}} \rangle$ remains globally small. For instance, approximately 60% of the sides of polygon for crushed particles are characterized by a ratio $(|\overrightarrow{e_{ij}}|/d) \leq 5 \times 10^{-2}$ while it is 80% for the spheres of S_{PS40} . Approximately 85% of the ratios $|\overrightarrow{e_{ij}}|/d$ are less than 10^{-1} for crushed particles, while 95% are less than 10^{-1} for the spheres of S_{PS40} .

However, significant differences between the two types of particles are brought out at the same time by Figs. 19(a), (c) and (e). On these three specific graphs, we observe as expected that the crushed particles from C_{PS40} are indeed characterized by:

- (i) an aspect ratio a_{ratio} ≥ 1.2 for one-third of the particles
- (ii) a larger portion of "small" angles than in the case of particles from S_{PS40} (~ 15% of α_f^{C_{PS40}} ≤ 155° against ≤ 4% of α_f^{S_{PS40}}),
- (iii) a larger portion of high eccentricity ($\sim 30\%$ of $(|\overrightarrow{e_{ij}}|/d)^{C_{PS40}} > 6 \times 10^{-2}$ against $\lesssim 10\%$ of $(|\overrightarrow{e_{ij}}|/d)^{S_{PS40}}$).

To sum up, all these observations show in fact that the shape of crushed particles in C_{PS40} do not deviate globally from a sphere. However, a small but non-negligible number of their sides are very different from spherical arcs, likely at least enough to induce the rheological differences between C_{PS40} and S_{PS40} observed in § 3.1. More precisely, these different measurements conducted to characterize the shape of particles tend to show that the rheological differences between C_{PS40} and S_{PS40} , if related to the particles shape, are mainly due to the three following quantities: a_{ratio} , α_i and $(|\vec{e_{ij}}|/d)$. We will see in the next section how these are all connected to each other and to μ_r .

4.2. Determination of the rolling friction coefficient.

4.2.1. Theoretical approach

Studies of granular media by Wensrich & Katterfeld (2012), Wensrich et al. (2014), Agarwal et al. (2021) and Tripathi et al. (2021) have shown that an order of magnitude of μ_r for usage in DEM simulations can often be obtained by measuring the ratio of the average contact eccentricity $\langle e \rangle$ to the projected particle diameter $d: \mu_r \approx \frac{\langle e \rangle}{d}$. This ratio is plotted in Fig.19(e) for the two studied suspensions in the present paper. We have measured $\langle |\vec{e}_{ij}|/d\rangle^{S_{PS40}} \sim 5 \times 10^{-2}$ and $\langle |\vec{e}_{ij}|/d\rangle^{C_{PS40}} \sim 10^{-1}$. Interestingly, one can observe that these values are in quite good agreement with the values previously predicted by the combination of the works of Singh et al. (2020) and the determination of $\phi_m(\Sigma_{12})$: $\mu_r^{\phi_m^{\infty}}|_{S_{PS40}} \approx 0.03 \pm 0.02$ and $\mu_r^{\phi_m^{\infty}}|_{C_{PS40}} \approx 0.10 \pm 0.01$, which confirms

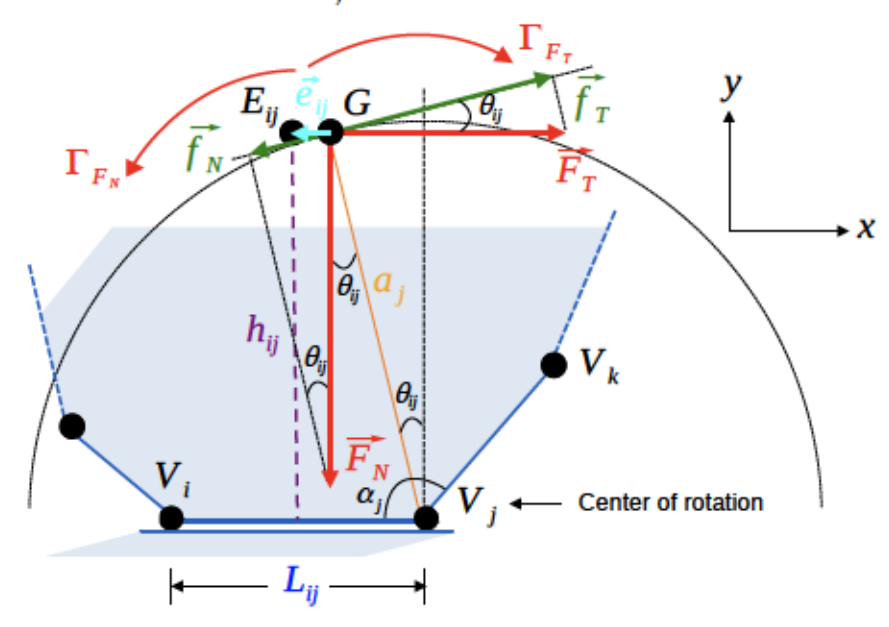


FIGURE 20. Schema based on the first sketch drawn in Fig.17 of a partial crushed particle (blue area), considered as an irregular convex polygon with a center of mass G. Here, the vertices V_i and V_j are the two vertices considered initially in direct contact with another particle. The forces $\overrightarrow{F_T}$ and $\overrightarrow{F_N}$ are the tangential and normal forces applied at G, respectively. The force $\overrightarrow{f_T}$ is the projection of $\overrightarrow{F_T}$ on the tangent passing by G of the circle of center V_j and radius a_j . In other words, $\overrightarrow{f_T}$ is the component of $\overrightarrow{F_T}$ which makes the polygon roll from left to right around V_j by applying a torque Γ_{F_T} . Similarly, $\overrightarrow{f_N}$ is the component of $\overrightarrow{F_N}$ which offers a resistance for the polygon to roll around V_j by applying a torque Γ_{F_N} . In this scenario, it is important to understand that the particle motion is from left to right and the particle can only roll (no sliding). In fact, a normal contact force opposing $\overrightarrow{F_N}$ and a sliding friction force opposing $\overrightarrow{F_T}$ are acting at the contact point V_j to prevent it from sliding or moving vertically, but they are not represented here for simplicity. The angle θ_{ij} corresponds to the angle between the vectors $\overrightarrow{GV_j}$ and $\overrightarrow{F_N}$.

the empirical proposition that the eccentricity can be used to estimate μ_r . However, a drawback of this method to calculate μ_r is that it is limited to particles whose shape does not deviate strongly from a sphere. For instance, it cannot be applied to regular polygonal particles (Estrada et al. 2011) for which we can expect obviously a higher rolling resistance than spheres despite the fact that their eccentricities are 0. Thus, we will follow and build upon the more fundamental approach of Estrada et al. (2011), in which μ_r is derived based on the torque required for rolling which in turn is related to the particle shape parameters.

Figure 20 displays a simple sketch of a crushed particle approximated here as an irregular convex polygon with center of mass G and number of sides n_s , rolling from the left to the right around one of its vertices (the one named V_f on the schematic in Fig.20) as a result of a tangential force $\overrightarrow{F_T}$ applied at the centroid G. We consider the conditions such that the irregular convex polygon/particle can only roll ($\mu_s >> \mu_r$, Estrada et al. 2008). As shown in Fig.20, a normal force $\overrightarrow{F_N}$ applied at G offers a resistance to the

particle's rolling, and rotation occurs only if:

$$\Gamma_{F_T} > \Gamma_{F_N}$$
 (4.4)

 Γ_{F_T} is the torque which tends to make the particle roll, and is defined as: $\Gamma_{F_T} = a_j \times \|\overrightarrow{f_T}\|$. Γ_{F_N} is the rolling resistance torque and is defined as: $\Gamma_{F_N} = a_j \times \|\overrightarrow{f_N}\|$. The forces $\overrightarrow{f_T}$ and $\overrightarrow{f_N}$ are the parts of the applied forces $\overrightarrow{F_T}$ and $\overrightarrow{F_N}$, respectively, which contribute to the corresponding torques, and are defined as (see Fig.20):

$$f_T = F_T \times \cos \theta_{ij}$$
 & $f_N = F_N \times \sin \theta_{ij}$ (4.5)

The angle θ_{ij} corresponds to the angle formed by the vectors $\overrightarrow{GV_j}$ and $\overrightarrow{F_N}$ when the polygon/particle rolls around its vertex V_j from left to right. By coupling eqs.(4.4) and (4.5), we obtain the following condition for the particle to roll around V_j from left to right:

$$F_T > F_N \times \tan \theta_{ij}$$
 (4.6)

Obviously, the value of θ_{ij} evolves during the rotation of the particle and, as a result, so does the force required to make the particle roll. Figure 21 displays a qualitative sketch of the horizontal force $\overrightarrow{F_T}$ that must be applied at the center of mass G as function of the rotation angle φ , in order to make an irregular polygon/crushed particle (composed of 5 sides) roll over its entire perimeter. One can then observe that the resistance for the particle to roll around one of its vertices is locally maximum at the start of the rotation around the given vertex.

According to the literature (Estrada et al. 2008, 2011; Singh et al. 2020), the rolling friction law between two grains of radii a_1 and a_2 defines the maximum torque transmitted by the contact from the rolling friction coefficient μ_r as: $\Gamma_{roll}^{\max} = \mu_r l F_N$, with $l = a_1 + a_2$. By assuming that a given particle rolls around its vertex V_j on a mirror particle in the studied suspensions S_{PS40} and C_{PS40} (consistent with suspensions roughly monodisperse and $a_{ratio} \sim 1$), we have $l = 2a_j$ which then leads to: $\Gamma_{roll}^{\max}/a_j = 2\mu_r F_N$. Thus, the applied tangential force F_T to roll a sphere equivalent to a crushed particle would have to be greater or equal to Γ_{roll}^{\max}/a_j (see Fig.2). Thanks to this equation and eq.(4.6), the static rolling friction coefficient associated with the vertex V_j when the particle rolls in a given direction (here from left to right), denoted $\mu_{r,s}^{ij}$, can be then described as (see Fig.20):

$$\mu_{r,s}^{ij} = (1/2) \tan \theta_{ij}^C$$
 with $\theta_{ij}^C = \max[\theta_{ij}]$ (4.7)

 θ_{ij}^C is defined as the maximum possible value reached by θ_{ij} when the particle rolls around a vertex V_j in a given direction. As shown in Figs. 20 and 21, this occurs when the side V_iV_j of the polygon is in contact with the mirror particle. Moreover, we want to point out that, through the parameter θ_{ij}^C , the static rolling friction coefficient related to it, $\mu_{r,s}^{ij}$, depends in fact on the length L_{ij} of the segment V_iV_j , the parameter e_{ij} and the height h_{ij} (see Fig.20) since:

$$\tan \theta_{ij}^{C} = \frac{(L_{ij}/2) + e_{ij}}{h_{ij}} \tag{4.8}$$

It is important to note that the value of e_{ij} is directly related to the vector $\overrightarrow{e_{ij}} = \overrightarrow{GE_{ij}}$, and can be positive or negative depending on the relative x-position of E_{ij} , G and V_j (see Fig.20) and the rolling direction:

If \$\overline{GE_{ij}}\$ points in the direction opposite to rolling, then \$e_{ij} < 0\$.

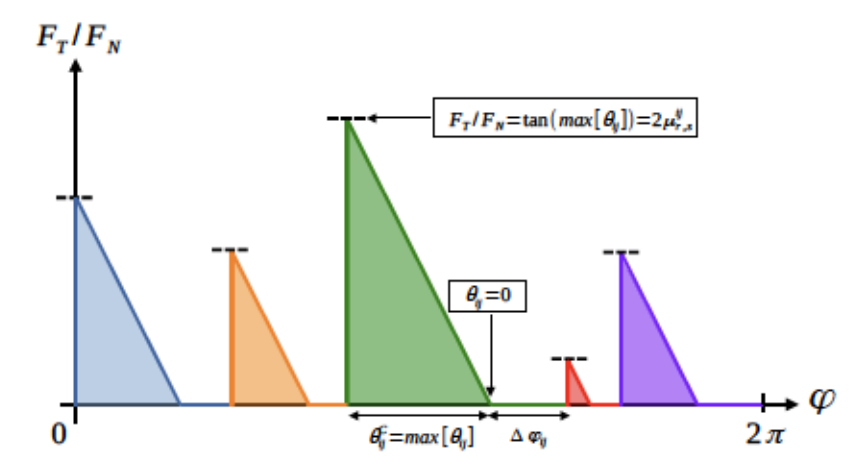


FIGURE 21. Qualitative sketch of the variation of the ratio F_T/F_N based on eq.(4.6) for an irregular convex polygon with 5 sides which rolls over its entire perimeter. Each colored peak labels the rotation of the given pentagon around one of its vertices. Each peak can have a different height because the pentagon is irregular. The height of one peak corresponds to the configuration where the contact with the second particle is "flat" (for instance, when V_i and V_j are both in contact with a second particle in Fig.20), for which $\theta_{ij} = \theta_{ij}^C$. Note that this corresponds to the position where the rolling resistance around the corresponding vertex is maximum. Then, after each colored peak, $F_T/F_N = 0$ over an angle, $\Delta \varphi$, with $\Delta \varphi_{ij} = \pi - (\alpha_j + \theta_{ij}^C)$. This is because $\overrightarrow{F_N}$ no longer induces a rolling resistance once G has been "vertically" aligned with the vertex/center of rotation ($\theta_{ij} = 0$). Thus, it is no longer necessary to apply a force $\overrightarrow{F_T}$ to continue rolling around the vertex in the same direction until the next vertex becomes the new contact point/center of rotation of the particle.

If \$\overline{GE_{ij}}\$ is the rolling direction, then \$e_{ij} > 0\$.

Another example which shows the importance of the relative x-position of these three points $(E_{ij}, G \text{ and } V_j)$ is that if G was located to the right of V_j in Fig.20 (with the particle rolling from left to right), then, $\mu_{r,s}^{ij} = 0$ (as qualitatively shown in Fig.21) since the force F_N applied on G no longer induces a resistance torque. We observe that the rolling resistance is larger when:

- the length of the side L_{ij} is large
- and/or e_{ij} increases the value of $(L_{ij}/2) + e_{ij}$
- and/or the height h_{ij} is small.

These observations from eq.(4.8) are actually quite intuitive. For instance, in the simple case of a regular $(e_{ij} = 0)$ 2D-polygon with 4 sides, we can easily imagine that it is harder to roll a cube $(\tan \theta_{ij}^C = 1)$ compared to a long rectangle laying on its small side (on the width, $\tan \theta_{ij}^C \to 0$). On the other hand, the long rectangle on its long side will be much harder to roll $(\mu_r^C) > 1$ when $\theta_{ij}^C \to 0^0$.

As observed in Fig.21, the irregular shape of 2D-polygons/crushed particles implies that the *static* rolling friction coefficient $\mu_{r,s}$ associated with a given irregular convex polygon/crushed particle is inhomogeneous in angular space. We have therefore chosen to define $\mu_{r,s}$ of a given particle as equal to the maximum value of $\mu_{r,s}^{ij}$:

$$\mu_{r,s} = \max \left[\mu_{r,s}^{ij} \right] \quad \forall (i,j) \in [0, n_s - 1]$$
 (4.9)

with:

- if
$$i < n_s - 1$$
, then $j = (i + 1)$
- if $i = n_s - 1$, then $j = 0$

The idea behind this choice follows the argument made by Estrada et al. (2008). We consider an irregular polygon laid on its side V_iV_i on a plane inclined with an angle θ_{ij} . In order to make the polygon roll down the inclined plane (i.e. to change its side in contact with the inclined plane), the angle of the slope must be larger than a critical value: $\theta_{ij} \gtrsim \theta_{ij}^C$. By rolling (without inertia), if the new critical angle θ_{jk}^C (associated with the new side V_1V_k in contact with the plane) is lower than the previous one (i.e. θ_{ij}^{C}), then rolling continues. However, if a subsequent segment of the polygon has a higher value of critical angle, the polygon stops rolling. In determining μ_r , s, we also consider the maximum resistance between the two possible directions of rotation.

Thus, the static rolling resistance is related to the torque required to initiate rolling (assuming the particle stopped rolling at its most resistant angle). But it is important to understand that another rolling resistance can be related to the work required to maintain rolling at a constant angular velocity. Both should be important in different parts of a sheared suspension (and at different times at the same location). Analogous to Estrada et al. (2011), this second rolling resistance can be determined by calculating the total work required to roll a non-spherical particle over its entire perimeter, P_p , and then balancing it with the total work of an equivalent sphere (of same perimeter P_p as the first one) with a resistance for rolling motion (i.e. a work balance instead of a torque balance). The resistance to rolling motion induced by the particle shape would be then characterized by a dynamic friction coefficient, $\mu_{r,d}$, instead of the static one, $\mu_{r,s}$. In Fig.21, it would be then determined from the total (colored) area under the curve F_T/F_N , instead of the maximum peak, and one can expect that $\mu_{r,d} \leqslant \mu_{r,s}$. We describe the method of calculating $\mu_{r,d}$ analogous to Estrada et al. (2011) in Appendix C, finally defined as:

$$\mu_{r,d} = \frac{1}{2P_p} \sum_{j=0}^{n_x - 1} \delta y_j' \tag{4.10}$$

with:
$$\quad \quad \cdot \; \delta y_j' = a_j - h_{ij} \; \text{if} \; a_i < \sqrt{L_{ij}^2 + h_{ij}^2},$$

- else $\delta y_i' = 0$.

In fact, one can note that $\mu_{r,d}$ is directly related to the averaged particle dilatancy, which is in agreement with the work of Estrada et al. (2011).

4.2.2. Image analysis results for the rolling friction coefficient

Figure 22 displays the measured distribution of (a) the maximum static rolling friction coefficient, $\mu_{r,s}$ and (b) the dynamic friction coefficient $\mu_{r,d}$, based on eqs.(4.9) and (4.10), respectively. Before discussing these graphs, we want to point out that the measurements on the "reference" perfectly smooth spheres (in green in Fig.22) give a maximum resolution (ie. lower limit for the values) on the order of 10^{-1} for $\mu_{r,s}$ and 10^{-2} for $\mu_{r,d}$.

Fig.22(a) displays the measured distribution of the static rolling friction coefficient, $\mu_{r,s}$. We observe that the values of $\mu_{r,s}$ associated with the crushed particles (in orange) are globally larger and more broadly distributed than the ones associated with the spheres from S_{PS40} (in blue). This result is quite intuitive since, for a given particle, we consider only the maximum value of $\mu_{r,s}^{ij}$ to determine $\mu_{r,s}$. As it is unlikely that the spherical part of a crushed particle is taken into account following this, the

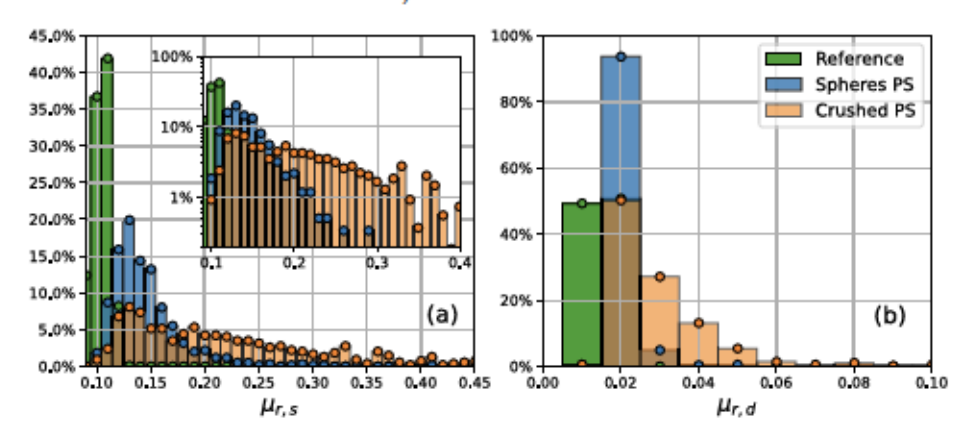


FIGURE 22. Distribution of (a) the static rolling friction coefficient, μ_r and (b) the dynamic rolling friction coefficient, $\mu_{r,d}$, both determined by image analysis for the reference perfectly smooth spheres (in green), the spherical particles composing S_{PS40} (in blue) and the crushed particles from C_{PS40} (in orange).

difference from spheres is then emphasized. One can even note that the values of $\mu_{r,s}^{S_{PS40}}$ slightly differ from the ones determined for perfectly smooth spheres (in green in Fig.22), which could come from real deformations of spheres composing S_{PS40} . The averaged value of $\mu_{r,s}$ for each suspension is measured to be: $\overline{\mu_{r,s}}|_{S_{PS40}}\approx 0.13$ and $\overline{\mu_{r,s}}|_{C_{PS40}}\approx 0.2$. Thus, on the one hand, we have $\mu_{r,s}^{S_{PS40}}<\mu_{r,s}^{C_{PS40}}$. On the other hand, it is actually quite satisfactory that $\mu_r^{\phi_m}\lesssim \mu_{r,s}$ for the two studied suspensions (we recall that we determined $\mu_r^{\phi_m}|_{S_{PS40}}\approx 0.03\pm 0.02$ and $\mu_r^{\phi_m}|_{C_{PS40}}\approx 0.10\pm 0.01$), since the static rolling friction coefficient, $\mu_{r,s}$, should characterize the maximum rolling resistance.

Figure 22(b) displays the measured distribution of the dynamic rolling friction coefficient, $\mu_{r,d}$, associated with the crushed particles of C_{PS40} (in orange) and the spheres of S_{PS40} (in blue). As expected, the values of $\mu_{r,d}$ are smaller than the values of $\mu_{r,s}$ for each studied suspension, and we still observe that $\mu_{r,d}^{S_{PS40}}$ is globally smaller and less distributed than $\mu_{r,d}^{C_{PS40}}$. We found the following averaged values: $\overline{\mu_{r,d}}|_{S_{PS40}} \approx 0.02$ and $\overline{\mu_{r,d}}|_{C_{PS40}} \approx 0.03$. Here, one can note that $\mu_{r,d} \lesssim \mu_r^{\phi_m}$ for each studied suspension.

Finally, the results of this study show that the globular/crushed PS particle geometry itself is enough to induce the rheological differences observed between C_{PS40} and S_{PS40} . To go further, it is quite satisfactory that $\mu_{r,d} \lesssim \mu_r^{\phi_m^\infty} \lesssim \mu_{r,s}$ for the two studied suspensions. We think that the experimental method described in the present paper to characterize the resistance to rolling motion induced by particle shape can be considered as another step to estimate the rolling friction coefficient for usage in DEM simulations, since it gives a framework for the value of μ_r for real suspensions made of non-spherical particles. We recall that, in agreement with the works of Agarwal et al. (2021) and Tripathi et al. (2021) in dry granular media, a more accurate estimation can be obtained by considering the particle eccentricity defined by e/d. However, two limits of this ratio exist: it cannot be considered for particles with a regular polygon shape (e = 0) or a shape that deviates too much from a sphere. Therfore, the novelty of the present work is then to give a way of estimating a framework of μ_r , particularly its upper (static) and lower (dynamic) bounds.

5. Concluding remarks

In this paper, two different but similar monodisperse suspensions have been sheared in a parallel plate rheometer in order to study their rheological behaviors and characterize their differences. More precisely, the main goal of the present paper was to study the influence of particle shape on the rheology of non-Brownian viscous frictional suspensions. Indeed, the rheology of suspensions composed of spherical particles has been extensively studied in the literature. However, understanding of the rheological behavior of more complex suspensions composed of particles with irregular shape, which are more common in nature, remains more elusive. We have made two different suspensions composed of the same solid polystyrene particles, separately dispersed in the same suspending Newtonian liquid. The only difference between the two lies in the shape of the particles present in each suspension: spheres in the first one, and crushed PS particles in the second one.

We have then characterized the rheological behavior of these different types of suspension by studying the variation of the jamming volume fraction with shear stress. Our main result shows that the suspension made of crushed particle is more viscous than the suspension made of spheres at small shear stress while the viscosity of the two suspensions becomes equivalent at large shear stress. This results in a stronger shear-thinning behavior for the suspension made of crushed particles. This observation is notably reflected by a jamming volume fraction smaller at low shear stress for crushed particles while it is of the same order of magnitude as that for spheres when shear stress increases.

To go further, we have tried to understand the physical mechanism behind this observation, obviously induced by the different particle shapes. The literature pointed out the influence of rolling resistance but two different origins could be related to it and have been proposed: changes of adhesive force strength with particles' local curvature and rolling resistance induced by locally normal contact forces acting at a non-spherical particle surface.

We have put forward two arguments which tend to demonstrate that adhesion is not important for the present rheological measurements. The first one has been to show that the applied shear stress in the present study is much larger than the yield stress of suspensions (spheres and crushed). The second (and main) argument has been based on conducting shear reversal experiments and measuring the minimum value of viscosity, η_{min} , and characteristic strains. The measurements of the same η_{min} in the two types of suspensions and characteristic strains typical for non-adhesive particles was in contradiction with what could be expected if adhesive forces had played a significant role.

The second explanation relates the shear-thinning behavior of both suspensions to a variable sliding friction, μ_s , while the larger viscosity at low shear stress for the non-spherical particles is assumed to be related to the particle shape. The recent numerical work of Singh *et al.* (2020) has shown that the rolling resistance of solid particles plays a predominant role determining the jamming volume fraction, ϕ_m , when the sliding friction coefficient is large ($\mu_s \gtrsim 0.5$), but has almost no effect when μ_s is small. A quick comparison on the suspensions made of PS spheres and crushed particles in the frictionless case (PS particles in an aqueous solution) has shown no rheological differences, which is consistent with the absence of impact of μ_r when $\mu_s \to 0$. We have

shown that it is possible to fit the variation of the jamming volume fraction with shear stress for both types of suspensions by the same variable sliding friction model (Lobry et al. 2019), simply by predicting a smaller value of the jamming volume fraction for crushed particles when the shear stress tends to 0 (ie. sliding friction coefficient grows "infinite"). The obtained value of ϕ_m^∞ (for which the predominant relative motion is rolling) from the fit (Lobry et al. 2019) coupled with the simulations of Singh et al. (2020) allowed us to obtain values of the apparent rolling friction coefficient for both types of suspension: $\mu_r^{\phi_m^\infty} = 0.03 \pm 0.02$ and $\mu_r^{\phi_m^\infty} = 0.10 \pm 0.01$ for spheres and crushed particles, respectively.

The last part of the present paper has been focused on an experimental estimation of the rolling friction coefficient for both types of particles studied in the present paper. Faced with the difficulty of performing a direct experimental measurement for such small non-spherical particles, we decided to use an image analysis process consisting of approximating particles as irregular convex 2D-polygons to measure the characterizing shape parameters such as aspect ratio, internal angle and eccentricity, and finally calculate the values of the static rolling friction coefficient associated with each side of each polygon, μ_r^{rj} . The static rolling friction coefficient of each particle, $\mu_{r,s}$, has been then defined as the maximum value of all $\mu_{r,s}^{tf}$ characterizing each particle. On the other hand, we have also determined the value of the dynamic friction coefficient, $\mu_{r,d}$, from the work needed to roll the particle over a distance equal to its own perimeter, analogous to Estrada et al. (2011). Therefore, $\mu_{r,d}$ can be then seen as an averaged value to characterize the shape-induced resistance of a particle to rolling motion based on the whole particle shape. Besides the fact that the particle geometry of the two studied suspension is enough to explain the rheological differences between the two, we have notably shown that the calculation of these two coefficient values ($\mu_{r,s}$ and $\mu_{r,d}$) gives a framework to estimate the value of μ_r for usage in numerical simulations.

Interestingly, a very good agreement with the recent works of Agarwal et al. (2021) and Tripathi et al. (2021) has been found and we confirmed that the eccentricity, defined as the ratio e/d, gives a very good estimation of the value of rolling resistance for usage in DEM simulations, as long as the particles shape does not deviate too much from a sphere, and that $e \neq 0$.

To go further, the next step would be to find a way to directly measure the rolling friction coefficient of the particles (as is done by AFM measurements for μ_s), instead of deducing it by an image analysis process. Other difficulties encountered here concern the irregular shape of crushed particles, and the diversity of irregular shapes, which might invalidate the 2D-approximation invoked here and make it harder to characterize the rolling resistance for irregular crushed particles. Being aware of this, we think it could be interesting to compare the numerical results of Singh et al. (2020) with more regularly defined shapes like cubic particles or other regular polygonal particles (for which e = 0). Small hard fibers ($a_{ratto} \leq 2$) could also be an interesting shape. One can note that the angularity explored through the crushed particles in the present study remains close to spheres ($\alpha_f \to 180^\circ$). Studying cubes or rectangular shapes may be then interesting to explore smaller internal angles domains ($\alpha_f \to 90^\circ$). It would have the second advantage of increasing the value of μ_r . Indeed, Singh et al. (2020) have shown that the influence of μ_r on ϕ_m is very large when $3 \times 10^{-2} \leq \mu_r \leq 3$. Cubes present this dual advantage of having a well-defined shape and an expected higher friction coefficient: μ_r is expected to

be between 0.1 (dynamic) and 0.5 (static), for which Singh et al. (2020) have predicted a much lower jamming fraction, $0.44 \lesssim \phi_m^{\infty} \lesssim 0.53$. Thus, determining ϕ_m^{∞} would show whether static or dynamic is more important. A rectangular shape ($a_{ratio} \lesssim 2$), it offers two very different side lengths and allows one to study further the influence of the angular dependency of μ_r .

Acknowledgements

We thank Yahya Al-Majali and Yasaman Madraki for their assistance with crushing the particles, and we thank F. Peters and A. Singh for fruitful discussions. We acknowledge A. Singh for sharing his data from Singh *et al.* (2020). This work was supported by National Science Foundation (NSF) (Grant No. CBET-1554044-CAREER & CBET-2210322). The authors report no conflict of interest.

Appendix A. Process to crush the polystyrene particles

Compression molding by a series of successive loading phases has been conducted in order to crush the spherical polystyrene particles. A sample of roughly $2-4\,ml$ of PS beads were put between two steel plates and compressed by a load equivalent to approximately $80\times 10^3\,kg$ (80 tons) for roughly 10 minutes. The particles of the given sample were then qualitatively observed under a microscope in order to check their appearance. The process was then repeated if the appearance of the particles was judged not satisfactory. Eventually, the loading operation on a given sample was repeated between 5 and 10 times.

Appendix B. The image analysis process

The image processing is performed as follows. Each image taken with a microscope is binarized with a local threshold whose value T(x,y) is calculated individually for each pixel (x,y). T(x,y) is a weighted sum (cross-correlation with a Gaussian window) of a $501 \times 501 \, px^2$ neighbourhood of the pixel (x,y) (see OpenCV: cv2.adaptiveThreshold / website: https://docs.opencv.org/2.4/index.html). A rough delimitation of each particle in the picture is thus detected. However, the pixels belonging to the interior of a particle, whose grey level can be similar to the background, can be incorrectly identified as not being part of the particle. As a result, the interior of particles is "filled" (see OpenCV: cv2.floodFill) in order to correct it. The projected particles and their well-defined contours (red pixels in Fig.18) are then detected through a watershed segmentation process (Vincent & Soille 1991, see OpenCV: cv2.watershed). Finally, the contour of each particle is approximated as an irregular convex envelope (see OpenCV: cv2.approxPolyDP, colored in blue in Fig.18) for which the (x,y)-coordinates of each vertex V_i (black dot except G in Fig.18) are known $(0 \le i \le n_s - 1$, with n_s the number of sides of the polygon).

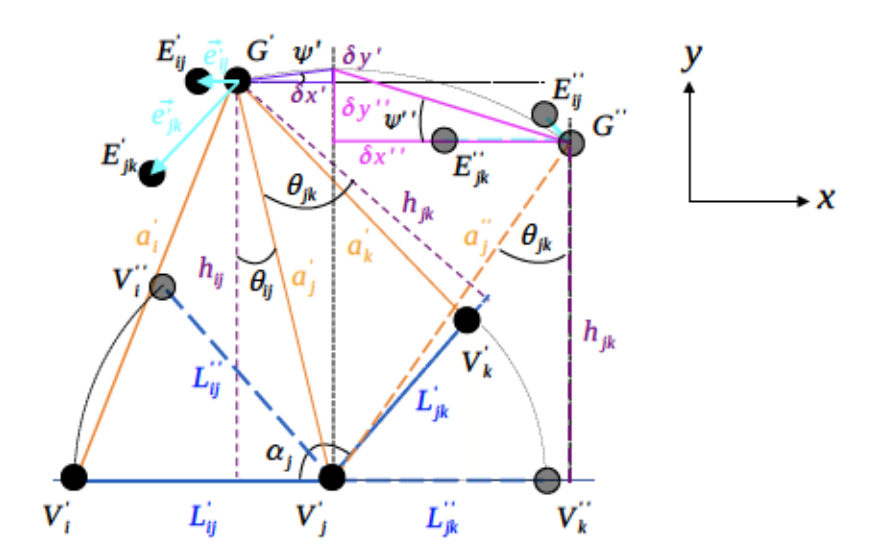


FIGURE 23. Sketch analogous to Fig.20 of a partial crushed particle, considered as an irregular convex polygon with a center of mass G. Two sides of the polygon/crushed particle, V_iV_j and V_jV_k , are outlined in dark blue. Tangential and normal forces, $\overrightarrow{F_T}$ and $\overrightarrow{F_N}$ (not represented here to avoid overloading the schema) respectively, are applied on the center of mass G of the particle as it is shown in Fig.20 to create a rolling motion from left to right around V_j . Under these conditions, V_i is the other vertex (with V_j) considered initially in direct contact with the mirrored particle, while V_k is the one which will be in contact at the end of the rotation around V_j . The initial (prime) location of each point is displayed with a black point and annotated ('), while the final (second) position is displayed with a transparent dot and annotated ("). Analogous to Fig.20, α_j corresponds to the internal angle of the polygon/particle at V_j ($\alpha_j = \widehat{V_iV_JV_k}$), θ_{ij} and θ_{jk} are the angles between the segments h_{ij} and GV_j , and h_{jk} and GV_j , respectively. The eccentricity for the sides V_iV_j and V_jV_k corresponds to the lengths $|\overrightarrow{e_{ij}}|/d$ and $|\overrightarrow{e_{jk}}|/d$, respectively. The angle ψ' (resp. ψ'') is the dilatancy angle when the particle rolls from the left to the right (resp. from the right to the left) around V_j .

Appendix C. Theoretical approach to determine the dynamic rolling friction coefficient

Let us consider that the center of mass G travels left to right over a horizontal distance which is given by: $\overrightarrow{x_G} = \delta x' + \delta x''$ (see Fig.23). Under these conditions, the work required to displace the crushed particle over this given distance can be calculated as:

$$W_p'|_j = \overrightarrow{F_N} \cdot \overrightarrow{y_G} = F_N \times \delta y_j'$$
 (C1)

 $\overrightarrow{y_G}$ is the vertical vector displacement of the centroid G for which the force F_N exerts a rolling resistance, and its norm is equal to $\delta y' = a_j - h_{ij}$. On the other hand, the work needed to displace a disk, characterized by a dynamic rolling friction coefficient $\mu_{r,d}$, over a distance equal to $\overrightarrow{x_G}$ is:

$$W_d = \overrightarrow{F_T} \cdot \overrightarrow{x_G} = 2\mu_{r,d} F_N \times (\delta x'_1 + \delta x''_1)$$
 (C2)

Assuming equal work, $W'_p|_{\mathcal{I}} = W_d$, we arrive at the following mapping for the dynamic friction coefficient associated with the rotation from left to right around $V_{\mathcal{I}}$:

$$\mu'_{r,d}|_{j} = \frac{1}{2} \left[\frac{\delta y'_{j}}{\delta x'_{j} + \delta x''_{j}} \right] \tag{C3}$$

where $\delta y'_{j} = a_{j} - h_{ij}$, $\delta x'_{j} = L_{ij}/2 + e_{ij}$ and $\delta x''_{j} = L_{jk}/2 + e_{jk}$ (with e_{ij} and e_{jk} positive or negative). Note that, in the case for which the particle rolls around V_{j} from the right to the left, $\mu_{r,d}$ is defined as:

$$\mu_{r,d}^{"}|_{j} = \frac{1}{2} \left[\frac{\delta y_{j}^{"}}{\delta x_{j}^{'} + \delta x_{j}^{"}} \right] \tag{C4}$$

where $\delta y_j'' = a_j - h_{jk}$. Obviously, if the polygon is regular $(L_{ij} = L_{jk}, e_{ij} = e_{jk} = 0, h_{ij} = h_{jk})$, then $\mu_{r,d} = \mu'_{r,d}|_{j} = \mu''_{r,d}|_{j}$ and we arrive at the following mapping between $\mu_{r,d}$ and the dilatancy angle $(\psi = \psi'_{j} = \psi''_{j} \quad \forall j \in [0 \quad n_s - 1])$, already found by Estrada et al. (2011):

$$\mu_{r,d} = (1/4) \tan \psi$$
 with $\psi = \frac{\pi}{2n_s}$ (C5)

In our case, the polygons are irregular and thus the required work to roll around one vertex is not the same for all the vertices of a particle, as is shown qualitatively in Figure 21 (the volume of each colored peak is different). Unlike the *static* friction coefficient, $\mu_{r,s}$, for which we have considered the maximum resistant torque to rolling motion, we define $\mu_{r,d}$ by considering the whole particle. The sum of the work for rolling over all vertices $W'_p|_j$ (or $W''_p|_j$) corresponds to the total work needed to displace a given particle over a distance equal to its perimeter P_p , and the value of the *dynamic* friction coefficient $\mu_{r,d}$ associated with the given particle can then be determined by the following equation:

$$\mu_{r,d} = \sum_{j=0}^{n_s - 1} \mu'_{r,d}|_{j} = \frac{1}{2P_p} \sum_{j=0}^{n_s - 1} \delta y'_{j}$$
 (C6)

whore

-
$$\delta y'_{j} = a_{j} - h_{ij}$$
 if $a_{i} < \sqrt{L_{ij}^{2} + h_{ij}^{2}}$,
- else $\delta y'_{i} = 0$.

REFERENCES

- ACRIVOS, ANDREAS, FAN, XIAOXING & MAURI, ROBERTO 1994 On the measurement of the relative viscosity of suspensions. *Journal of Rheology* 38 (5), 1285–1296.
- ACRIVOS, ANDREAS, MAURI, ROBERTO & FAN, X 1993 Shear-induced resuspension in a couette device. International journal of multiphase flow 19 (5), 797–802.
- AGARWAL, ARPIT, TRIPATHI, ANURAG, TRIPATHI, AMAN, KUMAR, VIMOD, CHAKRABARTY, ARIJIT & NAG, SAMIK 2021 Rolling friction measurement of slightly non-spherical particles using direct experiments and image analysis. Granular Matter 23 (3), 1–14.
- ARSHAD, MUHAMMAD, MAALI, ABDELHAMID, CLAUDET, CYRILLE, LOBRY, LAURENT, PETERS, FRANCOIS & LEMAIRE, ELISABETH 2021 An experimental study on the role of interparticle friction in the shear-thinning behavior of non-Brownian suspensions. *Soft Matter* 17 (25), 6088–6097, publisher: The Royal Society of Chemistry.
- BARNES, HA 1989 Shear-thickening ("dilatancy") in suspensions of nonaggregating solid particles dispersed in newtonian liquids. *Journal of Rheology* **33** (2), 329–366.
- BENDER, JONATHAN & WAGNER, NORMAN J 1996 Reversible shear thickening in monodisperse and bidisperse colloidal dispersions. Journal of Rheology 40 (5), 899–916.
- BLANC, FRÉDÉRIC, D'AMBROSIO, ENZO, LOBRY, LAURENT, PETERS, FRANÇOIS & LEMAIRE, ELISABETH 2018 Universal scaling law in frictional non-brownian suspensions. *Physical Review Fluids* 3 (11), 114303.
- BLANC, FRÉDÉRIC, LEMAIRE, ELISABETH, MEUNIER, ALAIN & PETERS, FRANÇOIS 2013 Microstructure in sheared non-brownian concentrated suspensions. *Journal of rheology* 57 (1), 273–292.
- BLANC, FRÉDÉRIC, PETERS, FRANÇOIS & LEMAIRE, ELISABETH 2011a Experimental signature of the pair trajectories of rough spheres in the shear-induced microstructure in noncolloidal suspensions. Physical review letters 107 (20), 208302.
- BLANC, FRÉDÉRIC, PETERS, FRANÇOIS & LEMAIRE, ELISABETH 2011b Local transient rheological behavior of concentrated suspensions. Journal of Rheology 55 (4), 835–854.
- BOYER, FRANÇOIS, GUAZZELLI, ÉLISABETH & POULIQUEN, OLIVIER 2011 Unifying suspension and granular rheology. Physical review letters 107 (18), 188301.
- BRIZMER, VICTOR, KLIGERMAN, YURI & ETSION, IZHAK 2007 Elastic-plastic spherical contact under combined normal and tangential loading in full stick. Tribology Letters 25 (1), 61-70.
- BROWN, ERIC, FORMAN, NICOLE A, ORELLANA, CARLOS S, ZHANG, HANJUN, MAYNOR, BENJAMIN W, BETTS, DOUGLAS E, DESIMONE, JOSEPH M & JAEGER, HEINRICH M 2010 Generality of shear thickening in dense suspensions. *Nature materials* 9 (3), 220–224.
- BROWN, ERIC & JAEGER, HEINRICH M 2012 The role of dilation and confining stresses in shear thickening of dense suspensions. *Journal of Rheology* 56 (4), 875–923.
- BROWN, ERIC & JAEGER, HEINRICH M 2014 Shear thickening in concentrated suspensions: phenomenology, mechanisms and relations to jamming. Reports on Progress in Physics 77 (4), 046602.
- CHATTÉ, GUILLAUME, COMTET, JEAN, NIGUÈS, ANTOINE, BOCQUET, LYDÉRIC, SIRIA, ALESSANDRO, DUCOURET, GUYLAINE, LEQUEUX, FRANÇOIS, LENOIR, NICOLAS, OVARLEZ, GUILLAUME & COLIN, ANNIE 2018 Shear thinning in non-brownian suspensions. Soft matter 14 (6), 879–893.
- CHOW, ANDREA W, SINTON, STEVEN W, IWAMIYA, JOSEPH H & STEPHENS, THOMAS S 1994 Shear-induced particle migration in couette and parallel-plate viscometers: Nmr imaging and stress measurements. *Physics of Fluids* 6 (8), 2561–2576.
- COMTET, JEAN, CHATTÉ, GUILLAUME, NIGUÈS, ANTOINE, BOCQUET, LYDÉRIC, SIRIA, ALESSANDRO & COLIN, ANNIE 2017 Pairwise frictional profile between particles determines discontinuous shear thickening transition in non-colloidal suspensions. *Nature* communications 8 (1), 1–7.
- Coussot, Philippe & Piau, Jean Michel 1994 On the behavior of fine mud suspensions. Rheologica acta 33 (3), 175–184.
- DAGOIS-BOHY, SIMON, HORMOZI, SARAH, GUAZZELLI, ELISABETH & POULIQUEN, OLIVIER 2015 Rheology of dense suspensions of non-colloidal spheres in yield-stress fluids. *Journal* of Fluid Mechanics 776.

- D'Ambrosio, Enzo, Blanc, Frédéric & Lemaire, Elisabeth 2021 Viscous resuspension of non-brownian particles: determination of the concentration profiles and particle normal stresses. *Journal of Fluid Mechanics* 911.
- DBOUK, TALIB, LOBRY, LAURENT & LEMAIRE, ELISABETH 2013 Normal stresses in concentrated non-brownian suspensions. *Journal of Fluid Mechanics* 715, 239.
- ESTRADA, NICOLAS, AZÉMA, EMILIEN, RADJAI, FARHANG & TABOADA, ALFREDO 2011 Identification of rolling resistance as a shape parameter in sheared granular media. *Physical Review E* 84 (1), 011306.
- ESTRADA, NICOLAS, TABOADA, ALFREDO & RADJAI, FARHANG 2008 Shear strength and force transmission in granular media with rolling resistance. *Physical Review E* **78** (2), 021301.
- FALL, ABDOULAYE, LEMAITRE, ANAEL, BERTRAND, FRANÇOIS, BONN, DANIEL & OVARLEZ, GUILLAUME 2010 Shear thickening and migration in granular suspensions. *Physical review letters* 105 (26), 268303.
- Fernandez, Nicolas, Mani, Roman, Rinaldi, David, Kadau, Dirk, Mosquet, Martin, Lombois-Burger, Hélene, Cayer-Barrioz, Juliette, Herrmann, Hans J, Spencer, Nicholas D & Isa, Lucio 2013 Microscopic mechanism for shear thickening of non-brownian suspensions. *Physical review letters* 111 (10), 108301.
- FRITH, WILLIAM J, D'HAENE, P, BUSCALL, R & MEWIS, JOANNES 1996 Shear thickening in model suspensions of sterically stabilized particles. Journal of rheology 40 (4), 531–548.
- GADALA-MARIA, F & ACRIVOS, ANDREAS 1980 Shear-induced structure in a concentrated suspension of solid spheres. *Journal of Rheology* 24 (6), 799–814.
- GADALA-MARIA, FRANCIS ARTURO 1979 THE RHEOLOGY OF CONCENTRATED SUSPENSIONS.. Stanford University.
- GALLIER, STANY, LEMAIRE, ELISABETH, PETERS, FRANÇOIS & LOBRY, LAURENT 2014 Rheology of sheared suspensions of rough frictional particles. *Journal of Fluid Mechanics* 757, 514-549.
- GALLIER, STANY, PETERS, FRANÇOIS & LOBRY, LAURENT 2018 Simulations of sheared dense noncolloidal suspensions: Evaluation of the role of long-range hydrodynamics. *Physical Review Fluids* 3 (4), 042301.
- GILBERT, DUNCAN 2021 Rôle des contacts adhésifs et frottants dans la rhéologie des suspensions non-browniennes. PhD thesis, Université Côte d'Azur.
- GILBERT, DUNCAN, VALETTE, RUDY & LEMAIRE, ELISABETH 2022 Impact of particle stiffness on shear-thinning of non-brownian suspensions. *Journal of Rheology* 66 (1), 161–176.
- GUY, BM, HERMES, MICHIEL & POON, WILSON CK 2015 Towards a unified description of the rheology of hard-particle suspensions. Physical review letters 115 (8), 088304.
- GUY, BM, RICHARDS, JA, HODGSON, DJM, BLANCO, E & POON, WCK 2018 Constraint-based approach to granular dispersion rheology. Physical review letters 121 (12), 128001.
- JOHNSON, KENNETH LANGSTRETH, KENDALL, KEVIN & ROBERTS, AAD 1971 Surface energy and the contact of elastic solids. Proceedings of the royal society of London. A. mathematical and physical sciences 324 (1558), 301–313.
- KEENTOK, MATTI & XUE, SHI-CHENG 1999 Edge fracture in cone-plate and parallel plate flows. Rheologica acta 38 (4), 321–348.
- KRIEGER, IRVIN M 1972 Rheology of monodisperse latices. Advances in Colloid and Interface science 3 (2), 111–136.
- LARSEN, RYAN J, KIM, JIN-WOONG, ZUKOSKI, CHARLES F & WEITZ, DAVID A 2010 Elasticity of dilatant particle suspensions during flow. *Physical Review E* 81 (1), 011502.
- LE, ANH VU NGUYEN, IZZET, ADRIEN, OVARLEZ, GUILLAUME & COLIN, ANNIE 2023 Solvents govern rheology and jamming of polymeric bead suspensions. Journal of Colloid and Interface Science 629, 438–450.
- LOBRY, LAURENT, LEMAIRE, ELISABETH, BLANC, FRÉDÉRIC, GALLIER, STANY & PETERS, FRANÇOIS 2019 Shear thinning in non-brownian suspensions explained by variable friction between particles .
- LOOTENS, DIDIER, VAN DAMME, HENRI, HÉMAR, YACINE & HÉBRAUD, PASCAL 2005 Dilatant flow of concentrated suspensions of rough particles. Physical review letters 95 (26), 268302.
- MADRAKI, YASAMAN, HORMOZI, SARAH, OVARLEZ, GUILLAUME, GUAZZELLI, ELISABETH & POULIQUEN, OLIVIER 2017 Enhancing shear thickening. Physical Review Fluids 2 (3), 033301.

- MADRAKI, Y, OAKLEY, A, NGUYEN LE, A, COLIN, A, OVARLEZ, G & HORMOZI, S 2020 Shear thickening in dense non-brownian suspensions: Viscous to inertial transition. *Journal of Rheology* 64 (2), 227–238.
- MADRAKI, YASAMAN, OVARLEZ, GUILLAUME & HORMOZI, SARAH 2018 Transition from continuous to discontinuous shear thickening: An excluded-volume effect. *Physical review letters* 121 (10), 108001.
- MARANZANO, BRENT J & WAGNER, NORMAN J 2001a The effects of interparticle interactions and particle size on reversible shear thickening: Hard-sphere colloidal dispersions. *Journal* of Rheology 45 (5), 1205–1222.
- MARANZANO, BRENT J & WAGNER, NORMAN J 2001b The effects of particle size on reversible shear thickening of concentrated colloidal dispersions. The Journal of chemical physics 114 (23), 10514–10527.
- MARI, ROMAIN, SETO, RYOHEI, MORRIS, JEFFREY F & DENN, MORTON M 2014 Shear thickening, frictionless and frictional rheologies in non-brownian suspensions. *Journal of Rheology* 58 (6), 1693–1724.
- MERHI, DIMA, LEMAIRE, ELISABETH, BOSSIS, GEORGES & MOUKALLED, FADL 2005 Particle migration in a concentrated suspension flowing between rotating parallel plates: Investigation of diffusion flux coefficients. *Journal of Rheology* 49 (6), 1429–1448.
- MUELLER, S, LLEWELLIN, EW & MADER, HM 2010 The rheology of suspensions of solid particles. Proceedings of the Royal Society A: Mathematical, Physical and Engineering Sciences 466 (2116), 1201–1228.
- Ness, Christopher & Sun, Jin 2016 Two-scale evolution during shear reversal in dense suspensions. *Physical Review E* **93** (1), 012604.
- OVARLEZ, GUILLAUME, BERTRAND, FRANÇOIS & RODTS, STÉPHANE 2006 Local determination of the constitutive law of a dense suspension of noncolloidal particles through magnetic resonance imaging. *Journal of rheology* 50 (3), 259–292.
- OVARLEZ, GUILLAUME, MAHAUT, FABIEN, DEBOEUF, STÉPHANIE, LENOIR, NICOLAS, HORMOZI, SARAH & CHATEAU, XAVIER 2015 Flows of suspensions of particles in yield stress fluids. Journal of rheology 59 (6), 1449–1486.
- Pantina, John P & Furst, Eric M 2005 Elasticity and critical bending moment of model colloidal aggregates. *Physical review letters* **94** (13), 138301.
- Peters, François, Ghigliotti, Giovanni, Gallier, Stany, Blanc, Frédéric, Lemaire, Elisabeth & Lobry, Laurent 2016 Rheology of non-brownian suspensions of rough frictional particles under shear reversal: A numerical study. *Journal of rheology* 60 (4), 715–732.
- PHILLIPS, RONALD J, ARMSTRONG, ROBERT C, BROWN, ROBERT A, GRAHAM, ALAN L & ABBOTT, JAMES R 1992 A constitutive equation for concentrated suspensions that accounts for shear-induced particle migration. *Physics of Fluids A: Fluid Dynamics* 4 (1), 30–40.
- PINE, DAVID J, GOLLUB, JERRY P, BRADY, JOHN F & LESHANSKY, ALEXANDER M 2005 Chaos and threshold for irreversibility in sheared suspensions. Nature 438 (7070), 997–1000.
- RASHEDI, AHMADREZA, OVARLEZ, GUILLAUME & HORMOZI, SARAH 2020 Engineered transparent emulsion to optically study particulate flows in yield stress fluids. Experiments in Fluids 61 (2), 1–13.
- RICHARDS, JAMES A, GUY, BEN M, BLANCO, ELENA, HERMES, MICHIEL, POY, GUILHEM & POON, WILSON CK 2020 The role of friction in the yielding of adhesive non-brownian suspensions. *Journal of Rheology* 64 (2), 405–412.
- SAINT-MICHEL, BRICE, MANNEVILLE, SÉBASTIEN, MEEKER, STEVEN, OVARLEZ, GUILLAUME & BODIGUEL, HUGUES 2019 X-ray radiography of viscous resuspension. *Physics of Fluids* 31 (10), 103301.
- SARABIAN, MOHAMMAD, FIROUZNIA, MOHAMMADHOSSEIN, METZGER, BLOEN & HORMOZI, SARAH 2019 Fully developed and transient concentration profiles of particulate suspensions sheared in a cylindrical couette. arXiv preprint arXiv:1906.03068.
- SCHATZMANN, MARKUS, FISCHER, PETER & BEZZOLA, GIAN RETO 2003 Rheological behavior of fine and large particle suspensions. Journal of Hydraulic Engineering 129 (10), 796–803.
- Seto, Ryohei, Mari, Romain, Morris, Jeffrey F & Denn, Morton M 2013 Discontinuous

- shear thickening of frictional hard-sphere suspensions. Physical review letters 111 (21), 218301.
- SINGH, ABHINENDRA, MARI, ROMAIN, DENN, MORTON M & MORRIS, JEFFREY F 2018 A constitutive model for simple shear of dense frictional suspensions. *Journal of Rheology* 62 (2), 457–468.
- SINGH, ABHINENDRA, NESS, CHRISTOPHER, SETO, RYOHEI, DE PABLO, JUAN J & JAEGER, HEINRICH M 2020 Shear thickening and jamming of dense suspensions: the "roll" of friction. Physical Review Letters 124 (24), 248005.
- SNOOK, BRADEN, BUTLER, JASON E & GUAZZELLI, ÉLISABETH 2016 Dynamics of shear-induced migration of spherical particles in oscillatory pipe flow. *Journal of Fluid Mechanics* 786, 128.
- Sosio, Rosanna & Crosta, Giovanni B 2009 Rheology of concentrated granular suspensions and possible implications for debris flow modeling. Water resources research 45 (3).
- TRIPATHI, AMAN, KUMAR, VIMOD, AGARWAL, ARPIT, TRIPATHI, ANURAG, BASU, SAPRATIV, CHAKRABARTY, ARIJIT & NAG, SAMIK 2021 Quantitative dem simulation of pellet and sinter particles using rolling friction estimated from image analysis. *Powder Technology* 380, 288-302.
- VANCE, KIRK, SANT, GAURAV & NEITHALATH, NARAYANAN 2015 The rheology of cementitious suspensions: a closer look at experimental parameters and property determination using common rheological models. Cement and Concrete Composites 59, 38–48.
- VÁZQUEZ-QUESADA, ADOLFO, MAHMUD, ARIF, DAI, SHAOCONG, ELLERO, MARCO & TANNER, ROGER I 2017 Investigating the causes of shear-thinning in non-colloidal suspensions: Experiments and simulations. Journal of Non-Newtonian Fluid Mechanics 248, 1–7.
- VÁZQUEZ-QUESADA, ADOLFO, TANNER, ROGER I & ELLERO, MARCO 2016 Shear thinning of noncolloidal suspensions. Physical review letters 117 (10), 108001.
- VINCENT, LUC & SOILLE, PIERRE 1991 Watersheds in digital spaces: an efficient algorithm based on immersion simulations. IEEE Computer Architecture Letters 13 (06), 583–598.
- WENSRICH, CM & KATTERFELD, A 2012 Rolling friction as a technique for modelling particle shape in dem. Powder Technology 217, 409-417.
- WENSRICH, CM, KATTERFELD, A & SUGO, D 2014 Characterisation of the effects of particle shape using a normalised contact eccentricity. Granular Matter 16 (3), 327–337.
- VAN DER WERFF, JC & DE KRUIF, CG 1989 Hard-sphere colloidal dispersions: the scaling of rheological properties with particle size, volume fraction, and shear rate. *Journal of Rheology* 33 (3), 421–454.
- WILDEMUTH, CR & WILLIAMS, MC 1984 Viscosity of suspensions modeled with a shear-dependent maximum packing fraction. Rheologica acta 23 (6), 627–635.
- Wyart, Mattheu & Cates, Micheal E 2014 Discontinuous shear thickening without inertia in dense non-brownian suspensions. *Physical review letters* 112 (9), 098302.
- Yoshimura, Ann & Prud'homme, Robert K 1988 Wall slip corrections for couette and parallel disk viscometers. *Journal of Rheology* 32 (1), 53-67.
- ZARRAGA, ISIDRO E, HILL, DAVIDE A & LEIGHTON JR, DAVID T 2000 The characterization of the total stress of concentrated suspensions of noncolloidal spheres in newtonian fluids. *Journal of Rheology* 44 (2), 185–220.
- ZHOU, JAMES ZQ, UHLHERR, PETER HT & LUO, FANG TUNAN 1995 Yield stress and maximum packing fraction of concentrated suspensions. Rheologica acta 34 (6), 544–561.